Thermodynamic optimisation of the performance of a parabolic trough receiver using synthetic oil-Al_2O_3 nanofluid

Aggrey Mwesigye[1†], Zhongjie Huan[1], Josua P. Meyer[2]

[1]Department of Mechanical Engineering, Mechatronics and Industrial Design, Tshwane University of Technology, Private Bag X680, Pretoria, 0001, South Africa

[2]Department of Mechanical and Aeronautical Engineering, University of Pretoria Private Bag X20, Hatfield 0028, South Africa

Abstract

In this paper, results of a thermodynamic analysis using the entropy generation minimisation method for a parabolic trough receiver tube making use of a synthetic oil-Al_2O_3 nanofluid as a heat transfer fluid are presented. A parabolic trough collector system with a rim angle of 80^o and a concentration ratio of 86 was used. The temperature of the nanofluid considered was in the range of 350 K to 600 K. The nanofluid thermal physical properties are temperature dependent. The Reynolds number varies from 3 560 to 1 151 000, depending on the temperature considered and volume fraction of nanoparticles in the base fluid. Nanoparticle volume fractions in the range $0 \leq \phi \leq 8\%$ were used. The local entropy generation rates due to fluid flow and heat transfer were determined numerically and used for the thermodynamic analysis. The study shows that using nanofluids improves the thermal efficiency of the receiver by up to 7.6%. There is an optimal Reynolds number at each inlet temperature and volume fraction for which the entropy generated is a minimum. The optimal Reynolds number decreases as the volume fraction increases. There is also a Reynolds number at every inlet temperature and volume fraction beyond which use of nanofluids is thermodynamically undesirable.

Key words

Entropy generation, nanofluid, optimal Reynolds number, parabolic trough receiver, thermodynamic analysis.

[†] Corresponding author: Tel: +27 12 382-4469, fax: +27 12 382-5602
Email address:mwesigyea@tut.ac.za
amwesigye@gmail.com

Nomenclature

a	Parabolic trough aperture width, m
A_c	Cross-section area, m^2
Be	Bejan number = entropy generated due to heat transfer/total entropy generated
C_1, C_2, C_μ	Turbulent model constants
c_f	Coefficient of friction
c_p	Specific heat capacity, J kg^{-1} K^{-1}
C_R	Concentration ratio
D	Tube diameter, m
d_{gi}	Glass cover inner diameter, m
d_{go}	Glass cover outer diameter, m
d_{ri}	Absorber tube inner diameter, m
d_{ro}	Absorber tube outer diameter, m
f	Darcy friction factor
f_f	Fanning friction factor
f_p	Focal length, m
G	Mass flux, kg s^{-1} m^{-2}
G_k	Generation of turbulent kinetic energy due to mean velocity gradients, kg $m^{-1}s^{-3}$
h	Heat transfer coefficient, W $m^{-2}K^{-1}$
h_w	Outer glass cover heat transfer coefficient, W $m^{-2}K^{-1}$
I_b	Direct normal irradiance, W m^{-2}
k	Turbulent kinetic energy, m^2 s^{-2}
L	Length, m
$\dot{m}$	Mass flow rate, kg s^{-1}
Nu	Nusselt number
P	Pressure, Pa
Pr	Prandtl number
q'	Rate of heat transfer per unit meter, W m^{-1}
q''	Heat flux, W m^{-2}
$\dot{q}_u$	Useful heat gain, W
Re	Reynolds number

Re_{th}	Reynolds number beyond which the use of nanofluids makes no thermodynamic case
S	Modulus of the mean rate-of-strain tensor, s^{-1}
S_{ij}	Rate of linear deformation tensor, s^{-1}
S_{gen}	Entropy generation rate due to heat transfer and fluid friction in the receiver, W K^{-1}
S'_{gen}	Entropy generation per unit length of the receiver, W m^{-1} K^{-1}
S'''_{gen}	Volumetric entropy generation, W $m^{-3}K^{-1}$
$(S'''_{gen})_F$	Volumetric entropy generation due to fluid friction, W $m^{-3}K^{-1}$
$(S'''_{gen})_H$	Volumetric entropy generation due to heat transfer, W $m^{-3}K^{-1}$
$S'''_{PROD,VD}$	Entropy production by direct dissipation, W $m^{-3}K^{-1}$
$S'''_{PROD,TD}$	Entropy production by turbulent dissipation, W $m^{-3}K^{-1}$
$S'''_{PROD,T}$	Entropy production by heat transfer with mean temperatures, W $m^{-3}K^{-1}$
$S'''_{PROD,TG}$	Entropy production by heat transfer with fluctuating temperatures, W $m^{-3}K^{-1}$
T	Temperature, K
u_m	Mean flow velocity, m s^{-1}
u_i,u_j	Velocity components, m s^{-1}
u',v',w'	Velocity fluctuations, m s^{-1}
u_τ	Friction velocity ($u_\tau = \sqrt{\tau_w / \rho}$), m s^{-1}
V	Volume, m^3
$\dot{V}$	Volumetric flow rate, m^3 s^{-1}
$\dot{W}_p$	Pumping power, W
x_i, x_j	Spatial coordinates, m
x,y,z	Cartesian coordinates, m
y^+	Dimensionless wall coordinate
$-\rho\overline{u'_i u'_j}$	Reynolds stresses, N m^{-2}
ΔP	Pressure drop, Pa

Greek letters

α	Thermal diffusivity, m^2 s^{-1}
α_t	Turbulent thermal diffusivity, m^2 s^{-1}
α_{abs}	Absorber tube absorptivity
$\sigma_{h.t}$	Turbulent Prandtl number for energy

σ_{ε}	Turbulent Prandtl number for ε
σ_k	Turbulent Prandtl number for *k*
σ_{slope}	Collector slope error, mrad
σ_{mirror}	Collector specularity error, mrad
δ_{ij}	Kronecker delta
ε	Turbulent dissipation rate, $m^2 s^{-3}$
ε_g	Glass cover emissivity
η	Turbulence model parameter = Sk/ε
η_{th}	Thermal efficiency, %
η_{el}	Electrical efficiency, %
ϕ	Nanoparticle volume fraction in the base fluid, %
φ_r	Rim angle, degrees
θ	Absorber tube circumferential angle, degrees
$\tilde{\Theta}$	Dimensionless inlet temperature
ρ	Density, $kg\ m^{-3}$
ρ	Mirror reflectivity
τ_w	Wall shear stress, $N\ m^{-2}$
τ_g	Glass cover transmissivity
λ	Fluid thermal conductivity, $W\ m^{-1}\ K^{-1}$
λ_{eff}	Fluid effective thermal conductivity, $W\ m^{-1}\ K^{-1}$
μ	Viscosity, Pa s
μ_t	Eddy viscosity, Pa s
ν	Kinematic viscosity, $m^2 s^{-1}$

Subscripts

amb	Ambient state
b	Base fluid
bulk	Bulk fluid state
F	Fluid friction irreversibility
H	Heat transfer irreversibility
i, j, k	General spatial indices
inlet	Inlet conditions
nf	Nanofluid

opt	Optimal
outlet	Outlet conditions
p	Nanoparticle
sky	Sky
t	Turbulent
w	Wall

Superscripts

_	Time averaged value
'	Fluctuation from mean value
~	Dimensionless parameter

1. Introduction

Harnessing solar energy for power generation is one the cleanest ways of meeting the increasing demand for modern energy services and extending the much-needed energy services to those with no access to it. Solar energy is generally widely available and is one of the renewable forms of energy with little or no impact on the environment. It has the potential to meet a significant portion of the world's energy demand [1].

Several methods are available for converting the sun's energy into electricity. These include photovoltaic (PV) systems and concentrated solar power (CSP) systems. CSP systems are advantageous, given that it is easier to incorporate energy storage for later use when there is no solar radiation. Several CSP technologies have been researched and developed, and others have been successfully deployed commercially. CSP technologies include the parabolic trough systems, parabolic dish systems, solar tower systems and linear Fresnel systems [2,3]. Of these technologies, the parabolic trough technology is the most commercially and technically developed CSP technology [3,4]. The technical and commercial success of these systems is attributed to the successful operation of the first solar electricity generation system (SEGS) in California's Mojave Desert [4]. These plants were built in the early 1980s and have been in operation ever since.

The major challenge with CSP systems is the high cost of electricity from these systems compared to electricity from coal plants. However, with several research and development initiatives [4,5], the cost of electricity from these systems has continued to decrease. With continued research and development efforts, the cost of electricity from these systems is predicted to become competitive with medium-sized gas plants in the near future [6].

Several research and development initiatives are underway to improve performance of CSP systems and make them cost competitive. The SunShot Initiative of the US Department of Energy is one of the many such initiatives [7]. Using higher concentration ratios is one of the areas that has a lot of potential for further cost reductions in parabolic trough systems [5,8]. Using higher concentration ratios means larger collector apertures, thus reducing the required length for the same aperture area. This, in turn, results in reduced connections and drives, thereby reducing the cost of installation, operation and maintenance of these systems. The Ultimate Trough® with an aperture of 7.5 m and a solar collector assembly length of 247 m

is one example of a parabolic trough system with a higher concentration ratio. Currently, it is the world's largest parabolic trough collector [8]. This collector is expected to reduce the solar field cost by 20 to 25% [8].

With increased concentration ratios, improved heat transfer performance of the receiver tubes becomes essential to reduce absorber tube temperatures, reduce absorber tube temperature gradients and, subsequently, reduce receiver thermal loss at these elevated temperatures [9,10]. It has also been shown in previous studies [11,12] that increasing concentration ratios increase the entropy generation rates in parabolic trough receivers, reducing their thermodynamic performance. This increase in entropy generation rates is attributed to the presence of large finite temperature differences in the receiver's absorber tubes as the concentration ratios increase [11,12] and as rim angles reduce to smaller values [12]. Thus, improved heat transfer performance of receiver tubes also plays a significant role in reducing these irreversibilities.

Enhancing convective heat transfer in the receiver's absorber tube is one of the ways to improve the receiver's heat transfer performance and address the concerns associated with high concentration ratios. Several investigations into heat transfer enhancement in parabolic trough receivers have been carried out and their potential for improving the receiver's heat transfer performance was demonstrated [13-17]. Most of these studies have investigated the use of passive heat transfer enhancement techniques to improve the performance of parabolic trough receivers. The studied enhancement mechanisms include surface modifications on the absorber tube, as well as the use of inserts.

The use of nanofluids has recently received significant attention for the enhancement of convective heat transfer. Nanofuids are thought to have an enormous potential to increase the heat transfer performance of heat transfer devices and heat exchangers beyond the capabilities of current working fluids. Nanofluids are simply engineered diluted colloidal suspensions of particles with sizes in the nanoscale range (less than 100 nm) in a base fluid [18]. The heat transfer performance that can be achieved with nanofluids greatly surpasses the performance of heat transfer liquids available today [19,20]. The heat transfer performance of nanofluids is attributed to their greatly enhanced thermal transport properties. Lee et al.[20] showed that using Al_2O_3 particles of about 13 nm in diameter at 4.3% volume fraction increased the thermal conductivity of water by about 15%. The review of studies on

the use nanofluids by Godson et al. [21] further underpins the heat transfer enhancement potential of nanofluids.

Some studies on using nanofluids for solar energy harvesting are available in literature. Javadi et al. [22] present an extensive review on the performance of solar collectors using nanofluids. From the review, particle concentration, temperature, size, dispersion and stability were shown to be the most effective parameters to increase the thermal conductivity of nanofluids.

In their study, Taylor et al. [23] used a conservative simplified analysis to compare a nano-based concentrated solar thermal system with a conventional one. They showed that nanofluids have excellent potential for power tower applications with 5 to 10% improvement in efficiency. Waghole et al. [24] experimentally investigated the heat transfer and friction factor of silver nanofluids in the absorber/receiver of a parabolic trough receiver with twisted tape inserts. Recently, Sokhansefat et al. [25] investigated heat transfer enhancement in a parabolic trough collector tube using a synthetic oil-Al_2O_3 nanofluid for the nanoparticle concentration less than 5% and operating temperatures of 300 K, 400 K and 500 K. They showed that the heat transfer performance increases as the volumetric concentration of nanoparticles increases. The heat transfer performance due to the use of the nanofluids was also found to decrease as the operating temperatures increased.

Despite the good thermal transport properties exhibited by nanofluids, there are several challenges associated with their use. Keblinski et al. [19] give highlights of some of the issues that need greater research attention. Godson et al. [21] mention some of the challenges that have hindered the widespread practical use of nanofluids. They mention rapid sedimentation, erosion, clogging and high pressure drop caused by inclusion of nanoparticles in the base fluid and cost or preparing nanofluids as some of the factors hindering the wide spread use of nanofluids. Similar to any new technology, it is anticipated that these challenges will be addressed in the near future with advances in research and development of nanotechnology. Moreover, despite these challenges, very small amounts of nanoparticles dispersed uniformly and suspended stably in the base fluid can improve the thermal properties of the base fluid substantially [21].

From the above literature review, it is evident that there is great potential for improved heat transfer performance by using nanofluids. Studies on heat transfer performance in parabolic

trough receivers using nanofluids are still limited. Furthermore, most studies available in literature use the first law of thermodynamics to evaluate the heat transfer performance with nanofluids. There are few studies using the second law for thermodynamic performance and thermodynamic optimisation of heat transfer devices using nanofluids. It is important that the conditions for which use of nanofluids is thermally and thermodynamically meaningful for any given application are established.

Besides, studies based on the second law of thermodynamics for assessing the quality of energy due to the use of nanofluids in parabolic trough systems are not common. The second law of thermodynamics provides the basis for characterising energy systems based on the quality of energy. The entropy generation minimisation method [26,27] is one of the methods based on the second law of thermodynamics that has become a valuable tool in the design of thermal systems. Therefore, the main purpose of this paper is to investigate the thermal and thermodynamic performance of a parabolic trough receiver using sylthern800-Al_2O_3 nanofluid with the entropy generation mimimisation method. The optimal Reynolds number and Reynolds number for which the use of nanofluids makes thermodynamic sense will be obtained and presented.

2. Physical model

The parabolic trough system consists of a mirror bent into a parabolic shape that collects the incident solar radiation and reflects it to a receiver tube placed at the focus of the parabola as shown in Figure 1. The collector considered in this study has a rim angle of 80^o, an aperture width of 6 m and a length of 5 m. The receiver tube consists of a steel absorber tube that is enclosed by a glass cover. In conventional receiver tubes used in power generation plants, the annulus space between the absorber tube and glass cover is evacuated to very low pressures of about 0.0103 Pa [4] to suppress convection heat loss. In addition, the absorber tube is selectively coated, making it highly absorptive to low-wavelength incoming radiation, with less emission of high-wavelength infrared radiation. The two-dimensional representations of the longitudinal and cross-sectional views of the receiver tube used in this study are shown in Figures 2(a) and 2(b) respectively. The receiver tube used in this study is similar to the SEGS LS-2 receiver. The absorber tube outer diameter is 70 mm and the glass cover outer diameter is 120 mm [4].

3. Numerical modelling

3.1 Governing equations

Flow inside the receiver's absorber tube is generally turbulent. The authors have also assumed steady-state conditions. Therefore, the general governing equations are the Reynolds averaged Navier-Stokes equations given by [28]:

Continuity

$$\frac{\partial\left(\rho\bar{u}_i\right)}{\partial x_i}=0 \tag{1}$$

Momentum equation

$$\frac{\partial}{\partial x_j}\left(\rho\bar{u}_i\bar{u}_j\right)=-\frac{\partial\bar{P}}{\partial x_i}+\frac{\partial}{\partial x_j}\left[\mu\left(\frac{\partial\bar{u}_i}{\partial x_j}+\frac{\partial\bar{u}_j}{\partial x_i}\right)-\frac{2}{3}\mu\frac{\partial\bar{u}_i}{\partial x_i}\delta_{ij}-\rho\overline{u_i'u_j'}\right] \tag{2}$$

Energy equation

$$\frac{\partial}{\partial x_j}\left(\rho\bar{u}_jC_p\bar{T}\right)=\frac{\partial}{\partial x_j}\left(\lambda\frac{\partial\bar{T}}{\partial x_j}+\frac{\mu_t}{\sigma_{h,t}}\frac{\partial\left(c_P\bar{T}\right)}{\partial x_j}\right)+\bar{u}_j\frac{\partial\bar{P}}{\partial x_j}+\left[\mu\left(\frac{\partial\bar{u}_i}{\partial x_j}+\frac{\partial\bar{u}_j}{\partial x_i}\right)-\frac{2}{3}\mu\frac{\partial\bar{u}_i}{\partial x_i}\delta_{ij}-\rho\overline{u_i'u_j'}\right]\frac{\partial\bar{u}_i}{\partial x_j} \tag{3}$$

The realisable *k-ε* model [29], an improvement of the commonly used standard k-ε models, was used for turbulence closure. The realisable *k-ε* model requires two additional equations for the turbulent kinetic energy (*k*) and turbulent dissipation rate (*ε*).

The Reynolds stresses in Equations 2 and 3 are related to strain according to [28]

$$-\overline{\rho u_i'u_j'}=\mu_t\left(\frac{\partial\bar{u}_i}{\partial x_j}+\frac{\partial\bar{u}_j}{\partial x_i}\right)-\frac{2}{3}\left(\rho k+\mu_t\frac{\partial\bar{u}_k}{\partial x_k}\right)\delta_{ij} \tag{4}$$

Where *k* is the turbulent kinetic energy given by [28]

$$k=\frac{1}{2}\left(\overline{u'^2}+\overline{v'^2}+\overline{w'^2}\right) \tag{5}$$

The transport equations for the turbulent kinetic energy and turbulent dissipation rate used in the realisable *k- ε,* as well as the turbulent kinetic energy (*k*), are given by [28,29]:

$$\frac{\partial}{\partial x_j}\left(\rho k\bar{u}_j\right)=\frac{\partial}{\partial x_j}\left[\left(\mu+\frac{\mu_t}{\sigma_k}\right)\frac{\partial k}{\partial x_j}\right]+G_k-\rho\varepsilon \tag{6}$$

and the turbulent dissipation rate (ε) is given by [28,29]

$$\frac{\partial}{\partial x_j}\left(\rho\varepsilon\bar{u}_j\right)=\frac{\partial}{\partial x_j}\left[\left(\mu+\frac{\mu_t}{\sigma_\varepsilon}\right)\frac{\partial \varepsilon}{\partial x_j}\right]+\rho C_1 S\varepsilon-\rho C_2\frac{\varepsilon^2}{k+\sqrt{\nu\varepsilon}} \tag{7}$$

Where G_k is the production of turbulent kinetic energy given by

$$G_k=-\rho\overline{u_i'u_j'}\frac{\partial\bar{u}_j}{\partial x_i} \tag{8}$$

From Equation 8, the production of turbulent kinetic energy (G_k) can be obtained as:

$$G_k=\mu_t S^2 \tag{9}$$

The eddy viscosity is given by [28]

$$\mu_t=\rho C_\mu\frac{k^2}{\varepsilon} \tag{10}$$

Detailed determination of C_μ is given in ANSYS® [28]. The model constants for the realisable k-ε model are

$C_1=\max\left[0.43,\frac{\eta}{\eta+5}\right]$, $\eta=S\frac{k}{\varepsilon}$, $S\equiv\sqrt{2S_{ij}S_{ij}}$, C_2=1.9, σ_k =1, σ_ε = 1.2. S_{ij} represents the rate of linear deformation of a fluid element. In total, there are nine components in three dimensions. Three of these components are linear elongation deformation components and six are shearing and deformation components [28].

3.2 Entropy generation

In this study, the entropy generation rates of interest are the ones due to heat transfer and fluid friction irreversibility. For convective heat transfer problems, entropy generation can be obtained from temperature and velocity fields, if known. This approach, where local entropy

generation rates are used, was shown to be superior to the one in which the entropy generation rate is obtained analytically, especially for complex geometries and complex boundary conditions [30]. In this study, the entropy generation was determined from the temperature and velocity fields from the results of the authors' computational fluid dynamics analysis as a sum of the heat transfer and fluid flow irreversibility according to the general equations presented by Kock and Herwig [31,32] as

$$S'''_{gen} = (S'''_{gen})_F + (S'''_{gen})_H \tag{11}$$

The entropy generation due to fluid friction $(S'''_{gen})_F$ is given as

$$(S'''_{gen})_F = S'''_{PROD,VD} + S'''_{PROD,TD} \tag{12}$$

Where:

$$S'''_{PROD,VD} = \frac{\mu}{\overline{T}}\left(\frac{\partial \overline{u}_i}{\partial x_j} + \frac{\partial \overline{u}_j}{\partial x_i}\right)\frac{\partial \overline{u}_i}{\partial x_j} \tag{13}$$

is the entropy generation by direct dissipation; and

$$S'''_{PROD,TD} = \frac{\rho\varepsilon}{\overline{T}} \tag{14}$$

is the entropy production by indirect (turbulent) dissipation.

The entropy generation due to heat transfer irreversibility $(S'''_{gen})_H$, is given as:

$$(S'''_{gen})_H = S'''_{PROD,T} + S'''_{PROD,TG} \tag{15}$$

Where:

$$S'''_{PROD,T} = \frac{\lambda}{\overline{T}^2}(\nabla \overline{T})^2 \tag{16}$$

is the entropy production by heat transfer due with mean temperatures and

$$S'''_{PROD,TG} = \frac{\alpha_t}{\alpha}\frac{\lambda}{\overline{T}^2}(\nabla\overline{T})^2 \tag{17}$$

is the entropy production with fluctuating temperatures, (λ) is the fluid thermal conductivity (α), and α_t are the thermal diffusivities.

Equations 11 to 17 give the entropy generation for each control volume. The total entropy generation rate for the entire computational domain with a fluid occupying V is given by:

$$S_{gen} = \iiint_V S'''_{gen} dV \tag{18}$$

Using the Bejan number, the relative contribution of each irreversibility to the total entropy generation rate can be shown. When the heat transfer irreversibility is dominant, $Be \approx 1$, and when the fluid friction irreversibility is dominant, $Be \approx 0$.

Analytically, the entropy generation in a tube subjected to constant heat flux is given by the expression presented by Bejan [27]. This expression relates the entropy generation to the heat transfer irreversibility and the fluid friction irreversibility as [27]

$$S'_{gen} = \frac{q'^2}{\pi\lambda T_{bulk}{}^2 Nu} + \frac{32\dot{m}^3 c_f}{\pi^2\rho^2 T_{bulk} D^5} \tag{19}$$

Where $\dot{m}$ is the flow rate, D is the tube diameter, q' is the heat transfer rate per unit length, $Nu = hD/\lambda$ with $h=q''/(T_w - T_{bulk})$, $c_f = (-dp/dx)\rho D/2G^2$, *with* $G = 4\dot{m}/\pi D^2$ and T_{bulk} is the bulk fluid temperature $(T_{inlet} + T_{outlet})/2$. The first term in Equation 19 is the entropy generation due to heat transfer irreversibility, and the second term is the heat transfer due to fluid friction irreversibility.

3.3 Thermophysical properties of nanofluids

The reliability and accuracy of the numerical results strongly depends on the correct specification of nanofluid properties. In this work, alumina (Al_2O_3), a commonly used and inexpensive nanoparticle, was used with Syltherm800, a commonly used synthetic oil in

parabolic trough systems, as the base fluid. In the synthetic oil-Al_2O_3 nanofluid mixture, the nanoparticles were taken to be 28 nm in diameter, similar to previous investigations [33,34]. As reported in these studies and generally in literature on nanofluids, the density is obtained using the classic formula for conventional solid-liquid mixtures, and the specific heat capacity is obtained assuming thermal equilibrium between particles and the surrounding liquid [33,34].

The nanofluid density is determined according to [33,34]

$$\rho_{nf} = (1-\phi)\rho_b + \phi\rho_p \tag{20}$$

The specific heat capacity is determined from [33-35]

$$c_{p_{nf}} = \frac{(1-\phi)c_{p_b}\rho_b + \phi c_{pp}\rho_p}{(1-\phi)\rho_b + \phi\rho_p} \tag{21}$$

Several models for determining the viscosity of nanofluids are available in literature. The dynamic viscosity used in this study is obtained from a model obtained by a precise least square curve fitting of experimental data [34-37]. According to this, the dynamic viscosity is given by

$$\mu_{nf} = \mu_b(123\phi^2 + 7.3\phi + 1) \tag{22}$$

For thermal conductivity, the Bruggeman model [34,38], which considers interaction among spherical particles with various concentrations of inclusion, was used. According to this, the thermal conductivity is given by [34,38]

$$\lambda_{nf} = 0.25\left[(3\phi-1)\lambda_p + (2-3\phi)\lambda_b + \sqrt{\Delta}\right] \tag{23}$$

$$\Delta = \left[(3\phi-1)\lambda_p + (2-3\phi)\lambda_b\right]^2 + 8\lambda_p\lambda_b \tag{24}$$

The thermal conductivity obtained with the Bruggeman model compares very well with the classic effective medium theory of Maxwell, which was shown to be accurate for well-dispersed particles [39].

The properties of the base fluid are temperature dependent. For this study, curve-fitted polynomials obtained using regression analysis from manufacturer data sheets [40] were used. The specific heat capacity (c_{pb}), the density (ρ_b) and the thermal conductivity (λ_p) are given by the polynomials given by Equations 25 to 27 respectively.

For $233.15 \leq T \leq 673$ K:

$$c_{pb} = 1.10787 + 1.70736 \times 10^{-3} T \ \ (kJ / kgK) \tag{25}$$

$$\rho_b = 1.2691 \times 10^{3} - 1.52115T + 1.79133 \times 10^{-3} T^2 - 1.67145 \times 10^{-6} T^3 \ \ (kg / m^3) \tag{26}$$

$$\lambda_b = 1.90134 \times 10^{-1} - 1.88053 \times 10^{-4} T \ \ (W / mK) \tag{27}$$

The viscosity is given by piecewise polynomials given by Equations 28 and 29.

For $233.15 \leq T \leq 343$ K:

$$\begin{aligned} \mu_b = {} & 5.14887 \times 10^{4} - 9.61656 \times 10^{2} T + 7.50207 T^2 - 3.12468 \times 10^{-2} T^3 + 7.32194 \times 10^{-5} T^4 \\ & - 9.14636 \times 10^{-8} T^5 + 4.75624 \times 10^{-11} T^6 \ \ (mPa.s) \end{aligned} \tag{28}$$

For $343 \leq T \leq 673.15$ K:

$$\begin{aligned} \mu_b = {} & 9.88562 \times 10^{1} - 7.30924 \times 10^{-1} T + 2.21917 \times 10^{-3} T^2 - 3.42377 \times 10^{-6} T^3 \\ & + 2.66836 \times 10^{-9} T^4 - 8.37194 \times 10^{-13} T^5 \ \ (mPa.s) \end{aligned} \tag{29}$$

The material properties of the Alumina nanoparticles (Al_2O_3) were taken to be constant [33,34] as shown in Table 1.

Table 1: Material properties for Alumina nanoparticles (Al_2O_3)

Material	ρ_p **(kg/m^3)**	c_{pp} **(J/kg K)**	μ_p **(Pa s)**	λ_p **(W /m K)**
Al_2O_3	3880	773	-	36

3.4 Heat flux and boundary conditions

To obtain an accurate solution for the receiver thermal model, it was essential to obtain an accurate representative heat flux distribution on the receiver's absorber tube. This was obtained using ray tracing in SolTrace [41]. In the ray tracing procedure, the sun shape was

specified as a pillbox with 10^8 as the maximum number of sun generated rays and 10^6 as the desired number of ray intersections. A slope error of 3 mrad and a specularity error of 0.5 mrad were used for the parabolic trough mirror. In actual systems, the average slope error is about 3.4 mrad [42]. The geometrical parameters of the parabolic trough system used are shown in Table 2. From ray tracing, the heat flux profile on the receiver's absorber tube at several rim angles and half the circumference of the absorber tube shown in Figure 2(b) is shown in Figure 3(a). The influence of slope errors on absorber tube heat flux distribution is also shown in Figure 3(b).

Generally, the heat flux distribution is non-uniform around the tube's circumference. The peak heat flux on the tube varies with the rim angle; it increases as the rim angle decreases. Rim angles lower than 60^o are shown to result in high heat flux peaks due to a high concentration of reflected rays on the lower half of the receiver. For this study, a rim angle of 80^o and an area concentration ratio of 86 were used. The area concentration ratio used is close to that in current systems, which is about 82 [4]. A rim angle of 80^o was shown to be an angle beyond which there are no significant reductions in heat flux peaks and entropy generation rates [12]. A direct normal irradiance (DNI) of 1 000 W/m^2 was used in this study. The obtained heat flux profile was hooked to a computational fluid dynamics code as a heat flux boundary condition using a user-defined function. The sample heat flux distribution at a rim angle of 80^o, concentration ratio of 86 slope error of 0 mrad and specularity error of 0 mrad on the receiver's absorber tube is shown in Figure 4.

The other boundary conditions used, as shown in Figure 2(a), were the following:

- Velocity inlet and pressure outlet at the absorber tube's inlet and outlet respectively
- No-slip and no-penetration for all walls
- Symmetry for the annulus space inlet and outlet – there is no flow in the receiver's annulus space
- A symmetry boundary condition for the entire receiver shown in Figure 2(b) as the section within $-90 \leq \theta \leq 90$
- For the outer wall of the receiver and the glass cover, a mixed radiation and convection boundary condition was used.

The radiation between the glass cover and the sky was obtained by the Stefan-Boltzmann law for a sky temperature given by $T_{sky} = 0.0552 T_{amb}^{1.5}$ [43]. Convection heat transfer was determined

by specifying a convection heat transfer coefficient as $h_w = V_w^{0.58} d_{go}^{-0.42}$ [44]. The wind speed (V_w) used was maintained at 2 m/s and the ambient temperature at 300 K for all cases. The other simulation parameters used are shown in Table 2.

Table 2: Simulation parameters used in this study

Parameter	Value	Parameter	Value
a	6 m	d_{ri}	0.066 m
L	5.0 m	d_{ro}	0.07 m
ρ	0.96	d_{gi}	0.115 m
α_{abs}	0.96	d_{go}	0.12 m
φ_r	80^o	τ_g	0.97
C_R	86	ϕ	0 - 8%
T_{inlet}	350 – 600 K	T_{amb}	300 K
Re	3.56×10^3 - 1.15×10^6	ε_g	0.86
σ_{slope}	3 mrad	σ_{mirror}	0.5 mrad

4. Numerical procedure and validation

4.1 Solution procedure

The solution to the governing equations, together with the boundary conditions, was obtained numerically using ANSYS® 14.5 [45]. The steps followed were the modelling of the geometry in ANSYS design modeler, the discretisation of the computational domain in ANSYS meshing and solving the governing equations together with the boundary conditions in ANSYS FLUENT [45], a computation fluid dynamics code based on the finite volume method. The SIMPLE algorithm that solves the governing equations in a segregated manner was used for pressure velocity coupling [46]. Second-order upwind schemes were used for the integration of the boundary conditions, together with the computational domain.

Convergence was obtained with scaled residuals less than 10^{-4} for the continuity equation, 10^{-6} for the momentum equations, turbulent kinetic energy and turbulent dissipation rate and 10^{-8} for the energy equation. In the simulations, a fully converged solution was essential for the accurate determination of the entropy generation rates. As such, the solution was left to run until the monitors for the residuals had ceased changing. In addition, the entropy generation was used to monitor convergence. The solution was considered converged when

the monitors for the volume integrated entropy generation rate remained unchanged for more than 150 successive iterations.

To ensure a mesh independent solution, the volume integrated entropy generation was used. The solution was taken to be mesh independent when the percentage change in entropy generation remained lower than 1% as the mesh size was reduced according to Equation 30. A mesh size of 6% of the absorber tube diameter in the stream-wise direction and 1.6% of the absorber tube diameter in the tube's cross-section was more than enough to give a mesh-independent solution for all simulations in this study.

$$\left| \frac{S_{gen}{}^{i} - S_{gen}{}^{i+1}}{S_{gen}{}^{i+1}} \right| \leq 0.01 \tag{30}$$

The indices *i* and *i+1* indicate the mesh before and after refinement respectively. Sample mesh used in this study is shown in Figure 5.

Prism layers were used to ensure values of the dimensionless wall coordinate, $y^+ \approx 1$. This was necessary to capture the high resolutions of flow variables near the tube walls for accurate heat transfer, fluid friction and entropy generation prediction, where $y^+ = yu_\tau/\nu$, in which ν is the fluid's kinematic viscosity, y is the distance from the wall, and u_τ is the friction velocity given by $u_\tau = \sqrt{(\tau_w / \rho)}$. For such low values of y^+, the enhanced wall treatment is recommended [45] and it was therefore adopted for this study.

4.2 Data reduction

The following parameters were used to present the results from this study.

The Reynolds number is given by

$$\mathrm{Re} = \rho_{nf} u_m d_{ri} / \mu_{nf} . \tag{31}$$

Where d_{ri} is the inner diameter of the receiver's absorber tube, ρ_{nf} is the nanofluid density and μ_{nf} is the nanofluid viscosity.

The average heat transfer coefficient is given by

$$h = q'' / (T_w - T_{bulk}) \tag{32}$$

Where T_w is the average wall temperature of the absorber tube and T_{bulk} is the bulk temperature of the fluid given by $(T_{inlet} + T_{outlet})/2$.

The average Nusselt number is given by

$$Nu = h d_{ri} / \lambda_{nf} \tag{33}$$

Where λ_{nf} is the thermal conductivity of the fluid.

The Darcy-Weisbach friction factor is defined as

$$f = \frac{\Delta P}{\frac{1}{2}\rho_{nf} \cdot u_m^2 \cdot \frac{L}{d_{ri}}} \tag{34}$$

To validate the results from the numerical model, several correlations and data available in literature were used. For friction factors in smooth tubes, the correlations used include the Petukhov's correlation [47], given as

$$f = \left(0.790 \ln \mathrm{Re} - 1.64\right)^{-2} \tag{35}$$

Blassius's correction for the Fanning friction factor (f_f) given as [48]

$$f_f = 0.079 \mathrm{Re}^{-0.25} \tag{36}$$

The Darcy friction factor (f) is obtainable from the Fanning friction factor by multiplying the Fanning friction factor by 4. This equation is valid for 4 000 < Re < 100 000 [48].

The other friction factor correlation used was obtained from Mwesigye et al. [17] on heat transfer performance in a parabolic trough receiver and is given as

$$f = 0.173\,\mathrm{Re}^{-0.1974} \tag{37}$$

For Nusselt numbers, correlations used include the Gnielinski's correlation for both low and high Reynolds numbers [47], given by

$$Nu = \frac{\left(f/8\right)\left(\mathrm{Re}-1000\right)Pr}{1+12.7\left(f/8\right)^{0.5}\left(Pr^{2/3}-1\right)} \tag{38}$$

For $0.5 \le Pr \le 2000$ and $3\times10^{3} \le \mathrm{Re} \le 5\times10^{6}$

The Dittus-Boelter correlation [47] for heating of the fluid given by

$$Nu = 0.023\mathrm{Re}^{0.8}\,\mathrm{Pr}^{0.4} \tag{39}$$

Mwesigye et al. [17] presented a Nusselt number correlation for a differentially heated absorber tube of a parabolic trough receiver as

$$Nu = 0.0104\,\mathrm{Pr}^{0.374}\,\mathrm{Re}^{0.885} \tag{40}$$

To validate the heat transfer performance with nanofluids, correlations obtained from experimental data were used. The Nusselt number correlation suggested by Pak and Cho [49] is given by

$$Nu = 0.021\mathrm{Re}^{0.8}\,\mathrm{Pr}^{0.5} \tag{41}$$

Equation 41 was derived for ranges of volume concentration (0-3%), Reynolds numbers (10^{4} – 10^{5}) and Prandtl numbers (6.54 – 12.33) [49]. Duangthongsuk and Wongwises [50] suggested a correlation for Nusselt number that includes the volume fraction as

$$Nu = 0.074\,\mathrm{Re}_{nf}^{\,0.707}\,\mathrm{Pr}^{0.385}\,\phi^{0.074} \tag{42}$$

Equation 42 was obtained for Water-TiO_2 nanofluid with volume fractions less than 1% and Reynolds numbers in the range 3 000 – 18 000. In the same study, Duangthongsuk and Wongwises [50] proposed a friction factor correlation as

$$f = 0.961\phi^{0.052}\,\mathrm{Re}^{-0.375} \tag{43}$$

For local determination of entropy generation rates, equations presented in Section 3.2 were used. The local entropy generation rates are then integrated over the entire computational domain according to Equation 18, to obtain the entropy generation rate for the entire computational domain.

4.3 Validation of numerical results

The results from our numerical analysis were validated for heat transfer, fluid friction and entropy generation using existing correlations. The heat transfer performance was validated for the case of ϕ = 0 with the Gnielinski correlation [47] given by Equation 38, the Dittus-Boelter correlation [47] given by Equation 39 and a correlation by Mwesigye et al. [17] given by Equation 40. As shown in the scatter plot in Figure 6, the present study results are shown to be in good agreement with the given correlations. However, significant variations were noted with the Dittus-Boelter correlation, especially at high Reynolds numbers. This is probably due to the significant temperature difference between the bulk fluid and the absorber tube wall at high Reynolds numbers. The Dittus-Boelter correlation is said to be a good approximation of the Nusselt number when the temperature difference between the bulk fluid and heat transfer surface is minimal [47].

The present study friction factors were compared with the friction factor correlations by Blasius [48], which is given by Equation 36, Petukhov [47], which is given by Equation 35 and a correlation from Mwesigye et al. [17], which is given by Equation 37. Excellent agreement was obtained, as shown in Figure 7. However, notable deviations are shown to exist with the Blasius correlation at high Reynolds numbers. This is because the Blasius correlation is valid for Reynolds numbers in the range 4000 < Re < 100 000 [48].

To validate the nanofluid models used, the Nusselt number correlations in Equations 41 and 42 were compared with results from the present study. The results used were selected to fall within the range of Prandtl numbers for which the equations were obtained. Heat transfer fluid properties evaluated at 550 K, 600 K and 650 K gave Prandtl numbers in the range 9.5 – 14.95 and were therefore used. Equation 41 gave the closest approximation compared to Equation 42, probably be due to the low Reynolds numbers used in obtaining Equation 42.

As shown in Figure 8(a), excellent agreement was achieved with the Pak and Cho [49] correlation (Equation 41), especially for Nusselt numbers at low values of Reynolds numbers. This is because the correlation was obtained for Reynolds numbers lower than 100 000. As the Reynolds numbers increase, the same trend exists, but the deviation of present study results from those obtained with the correlation increases. At Reynolds numbers lower than 500 000 the present study values are within ±8% of the experimental values. For fluid friction, values of Reynolds numbers and volume fractions close to those used in obtaining the correlation given in Equation 43 were used. As shown in Figure 8(b), good agreement was obtained for values in the range of Reynolds numbers for which the correlation was derived. For Reynolds numbers between 5 000 and 40 000, present study results are within ±10% of experimental values.

For the entire range of values used in this study, the Nusselt number can be obtained from the correlation

$$Nu = 0.008905\,\mathrm{Re}^{0.8966}\,\mathrm{Pr}^{0.3805}\,\tilde{\phi}^{-1.1836\times10^{-3}} \tag{44}$$

The volume fraction has been non-dimensionlised as $\tilde{\phi} = \phi / \phi_{ref}$, with ϕ_{ref} = 1%. This correlation was obtained using non-linear regression with R^2 = 0.999. It predicts the Nusselt number within ±4%. The correlation was obtained for 3 560 ≤ Re ≤ 1 151 000, $0 \le \phi \le 8\%$, $350 \le T_{inlet} \le 600$ K and 9.27 ≤ Pr ≤ 96.58. For the same range of values, the friction factor is given by

$$f = 0.2085\,\mathrm{Re}^{-0.2132}\,\tilde{\phi}^{1.0538\times10^{-2}} \tag{45}$$

For this friction factor correlation, R^2 = 0.97 and the correlation predicts the friction factor within ±8%.

The results of the entropy generation model were compared with the entropy generation values obtained from the analytical expression proposed by Bejan [27], given by Equation 19. The developed receiver thermal model was compared with data from Sandia National Laboratories. The validations of the receiver thermal model and the entropy generation model were presented in previous investigations by Mwesigye et al. [17,51] and good agreement was achieved in these studies. For the same experimental conditions used by Dudely et al. [52], the numerical results of the receiver thermal model were compared with experimental data for temperature gain and thermal efficiency. Agreement within ± 6.5% for most data points was obtained for both temperature gain and thermal efficiency.

5. Results and discussions

5.1 Heat transfer and fluid friction performance

Figures 9(a) to 9(c) show the heat transfer coefficient as a function of the Reynolds number and nanoparticle volume fraction at temperatures of 400 K, 500 K and 600 K respectively. As shown in the figures, the use of nanofluids gives better heat transfer performance compared to the case where only the base fluid is used (ϕ = 0%). The heat transfer coefficients continue to increase as the Reynolds number and nanoparticle volume fraction in the base fluid increase. The increase in heat transfer performance as Reynolds numbers increase can be attributed to a thinner boundary layer, lower absorber tube wall temperatures, as well as lower bulk temperatures at high Reynolds numbers. The increase in heat transfer performance as nanoparticle volume fraction increases can be attributed to the enhanced heat transfer properties of the fluid due to dispersion of nanoparticles in the base fluid.

From Figures 9(a) to 9(c), it can be seen that the heat transfer coefficient increases by as much as 76, 54 and 35% as the volume fraction increases from 0 to 8%, 0 to 6% and 0 to 4% respectively. The highest increase in heat transfer coefficients is shown to exist at high volume fractions, high Reynolds numbers and lowest fluid temperatures. It should be noted that, at a given flow rate, the Reynolds numbers increase as the fluid temperatures increase. The corresponding data points in Figures 9(a) to 9(c) represent the same flow rate, but the Reynolds number will change as the volume fraction and fluid temperature change, given the dependence of fluid properties on volume fraction and temperature. For example, the lowest Reynolds number in all the figures corresponds to a flow rate of 4.92 m^3/h. At this flow rate and ϕ = 0%, the Reynolds numbers are 6 710, 10 890, 17 000, 24 960, 34 330 and 44 520 at fluid temperatures of 350 K, 400 K, 450 K, 500 K, 550 K and 600 K respectively. For plots at different temperatures and volume fractions, the Reynolds numbers were obtained from flow rates that were varied in the range 4.92 m^3/h to 104 m^3/h.

As expected, the increase in heat transfer performance as volume fraction and Reynolds numbers increase is associated with an increase in the fluid friction that must be overcome and, hence, an increase in pumping power. Figures 10(a) to 10(c) show the pressure drop per unit metre ($\Delta P/L$) as a function of the Reynolds number and volume fraction at inlet temperatures of 400 K, 500 K and 600 K, respectively. The pressure drops are shown to increase as the volume fraction and Reynolds numbers increase. Increasing the concentration

of nanoparticles in the nanofluid makes the fluid denser and more viscous. This increases flow resistance and necessitates more pumping power. At the same flow rate, it can also be seen that the pressure drop reduces as the fluid temperatures increase. This is because the fluid becomes less dense and less viscous as temperatures increase. According to Figures 10(a) to 10(c), the pressure drop increases significantly as the volume fraction increases above 4%, especially at higher Reynolds numbers. As such, the increase in heat transfer performance should be sufficiently higher than the increase in pumping power for the use of nanofluids to make economic sense.

5.2 Thermal efficiency

To show the gain in thermal performance of a parabolic trough receiver with nanofluids, it is necessary to consider both the increase in performance and the associated increase in pumping power. The thermal efficiency of the system can be used for this purpose. In determining the thermal efficiency, the pumping power is subtracted from the useful heat energy. In addition, a value of electrical efficiency is introduced to convert the pumping power to the same form as the useful heat energy. Accordingly, the thermal efficiency is given as:

$$\eta_{th} = \frac{\dot{q}_u - \dot{W}_p / \eta_{el}}{I_b A_c} \tag{46}$$

The electrical efficiency of the power block η_{el} used in Equation 46 was taken as 32.7% [53], $\dot{q}_u = \dot{m} c_p (T_{outlet} - T_{inlet})$ and $\dot{W}_p = \dot{V} \Delta P$. Figures 11(a) to 11(c) show the thermal efficiency as a function of the Reynolds number and nanoparticle volume fraction at inlet temperatures of 400 K, 500 K and 600 K, respectively. From the figures, it is shown that the variation of the thermal efficiency follows different trends, depending on the inlet temperature considered. At low values of inlet temperature, the thermal efficiency continually decreases as the Reynolds number increases. At higher values of inlet temperature, the thermal efficiency increases as the Reynolds number increases, attains a maximum value and then decreases.

At low temperatures, the absorber tube temperatures are low and, therefore, receiver thermal loss is low, so that increasing the flow rates does not significantly affect the receiver thermal loss and thermal performance. However, since the fluid is denser and more viscous at low

temperatures, increasing the flow rates decreases the thermal efficiency due to increased pumping power. As temperatures increase, absorber tube temperatures, as well as receiver radiation losses, increase. As such, increasing flow rates reduce the absorber tube temperatures and thus radiation losses, thereby increasing receiver thermal efficiency. A further increase in flow rates leads to much higher pumping power requirements and the efficiency decreases. For all temperatures considered, beyond some flow rate, the thermal efficiency becomes lower than that in a receiver with only the base fluid as the volume fraction increases. This is because the increase in pumping power becomes higher than the gain in performance at higher Reynolds numbers and higher volume fractions.

The highest increase in thermal efficiency is about 7.6%. It exists at the lowest temperature and lowest flow rate considered in this study. This is probably because, for the same flow rate, the heat transfer performance is lower at lower temperatures due to poor heat transfer properties of the heat transfer fluid. As such, using nanofluids at such temperatures enhances the heat transfer properties of the fluid and improves the performance. Moreover, at higher temperatures, the fluid is much more turbulent at the same flow rate. Thus, the high pumping power requirements reduce the thermal efficiency. For higher fluid temperatures, reducing flow rates would ensure a significant increase in the thermal efficiency. Flow rates lower than 25 m^3/h result in reasonable improvement in receiver thermal efficiency for most fluid temperatures and volume fractions considered.

5.3 Thermodynamic analysis and optimisation

5.3.1 Heat transfer and fluid friction irreversibilities

The heat transfer and fluid friction irreversibilities are the two irreversibilities that contribute to the entropy generation rate in the receiver's absorber tube. These irreversibilities generally compete against one another. As the heat transfer irreversibility decreases, the fluid friction irreversibility increases. Figure 12 shows the variation of the two irreversibilities with the Reynolds numbers for an inlet temperature of 500 K and a volume fraction of 1%. The heat transfer irreversibility decreases as the Reynolds number and volume fraction increase due to improved heat transfer performance and, thus, reduced finite temperature differences. The increase in the fluid friction irreversibility as the Reynolds number and volume fraction increase is due to increased pressure drop from high resistance to fluid flow. The same trend is expected at any fluid temperature and volume fraction.

Figures 13 (a) and 13(b) show the entropy generation due to fluid friction and heat transfer respectively, as functions of the Reynolds number and volume fraction at an inlet temperature of 450 K. As shown, the heat transfer irreversibility decreases with increases in the Reynolds number and volume fraction due to improved heat transfer performance. The fluid friction irreversibility increases as the Reynolds number and volume fraction increase due to increased resistance to fluid flow. The increase in fluid friction irreversibility as volume fraction increases is shown to be much higher than the reduction in the heat transfer irreversibility. However, the magnitude of the heat transfer irreversibility is much higher than that of the fluid friction irreversibility.

As shown in Figure 13(a), the fluid friction irreversibility is very small at low Reynolds numbers. It increases as the Reynolds numbers increase, becoming higher and dominant at higher Reynolds numbers. The heat transfer irreversibility is higher than the fluid friction irreversibility at low Reynolds numbers and decreases with increasing Reynolds numbers and volume fraction. Accordingly, heat transfer enhancement should be considered in cases where heat transfer irreversibility is higher than fluid friction irreversibilities.

5.3.2 Bejan number

The contribution of each of the irreversibilities to the total entropy generation rate can be shown clearly by the Bejan number. The Bejan number as a function of the Reynolds number and volume fraction at inlet temperatures of 400 K and 600 K are shown in Figures 14 (a) and 14(b), respectively. The same trend exists at other inlet temperatures. As expected, the Bejan number decreases as the Reynolds number and volume fraction increase. This is mainly due to the increase in fluid friction irreversibility and reduction in the heat transfer irreversibility. The Bejan number also decreases as the inlet temperature increases. This is due to better heat transfer performance and reduced fluid friction as fluid temperatures increase at a given flow rate.

5.3.3 Thermodynamic optimisation

The total entropy generation rate is the sum of the fluid friction and heat transfer irreversibility. From the variation of the two irreversibilities discussed earlier, the total entropy generation rate is a minimum at a certain Reynolds number. Figures 15(a) to 15(c)

show the total entropy generation in the receiver as a function of the Reynolds number and volume fraction at inlet temperatures of 350 K, 450 K and 550 K respectively.

Figure 15 shows that there is an optimal Reynolds number (Re_{opt}) that minimises the entropy generation rate at every inlet temperature value and volume fraction. A closer look at the figure shows that the optimal Reynolds number decreases as the volume fraction increases. An increase in nanoparticle volume fraction results in improved heat transfer performance and, thus, less heat transfer irreversibility. However, the fluid friction irreversibility will increase as the volume fraction increases. A combination of these two decreases the optimal Reynolds number as the volume fraction decreases. Furthermore, it can be seen that there is a Reynolds number (Re_{th}) at which the entropy generation due to use of nanofluids becomes greater than that in a receiver with only the base fluid (ϕ = 0%). Beyond this Reynolds number (Re_{th}), further increases in Reynolds numbers make no thermodynamic sense. Additionally, it is also clear from the figures that entropy generation at lower fluid temperatures is lower than at high fluid temperatures for any given flow rate. This is mainly because heat transfer irreversibilities are high at low temperatures due to poor heat transfer fluid thermal transport properties. Moreover, the fluid becomes less dense as temperatures increase and low fluid friction irreversibility occurs.

Figure 16 shows the optimal Reynolds number as a function of volume fraction and inlet temperature. The optimal Reynolds number decreases as the nanoparticle volume fraction increases. Sufficient heat transfer performance is achievable with low flow rates and high nanoparticle volume fraction. Higher Reynolds numbers would result in increased fluid friction irreversibility and higher entropy generation rates. Given the variation of heat transfer fluid properties with temperature, higher temperatures generally result in higher Reynolds numbers compared to lower temperatures.

For the range of parameters considered, the optimal Reynolds number is given by:

$$\mathrm{Re}_{opt} = 5\,394\,186\tilde{\phi}^{1.2026\times10^{-3}}\tilde{\Theta}^{0.4883}\,\mathrm{Pr}^{-1.0695} \quad (47)$$

In Equation 47, the volume fraction has been non-dimensionlised as $\tilde{\phi} = \phi / \phi_{ref}$, with ϕ_{ref} = 1%. The inlet temperature is non-dimensionlised as $\tilde{\Theta} = T_{inlet} / T_{amb}$, with T_{amb} = 300 K.

R^2 = 0.998 for Equation 47 and predicts the optimal Reynolds number within 8%. However, about 90% of the values are within 4%. This equation was obtained for $1\% \le \phi \le 8\%$, $350\ \text{K} \le T_{inlet} \le 600\ \text{K}$ and the simulation parameters presented in Table 2.

Figure 17 shows the Reynolds number beyond which the use of nanofluids makes no thermodynamic sense (Re_{th}) as a function of volume fraction and inlet temperature. The same trend as that of the optimal Reynolds number is shown to exist. Re_{th} decreases as the volume fraction increases and as the inlet temperature decreases. At low volume fractions, the optimal Reynolds number and Re_{th} are not very distinct, as shown in Figures 15(a) and 15(b). However, Re_{th} becomes significantly higher than the optimal Reynolds number as the nanoparticle volume fraction is 4% and higher. The Reynolds number beyond which the use of nanofluids makes no thermodynamic sense can be obtained from the correlation given by:

$$\text{Re}_{th} = 1\,023\,833\tilde{\phi}^{0.02763}\tilde{\Theta}^{1.6259}\,\text{Pr}^{-0.7181} \tag{48}$$

R^2 = 0.999 for Equation 48 and predicts Re_{th} within 4%. This equation was obtained for $1\% \le \phi \le 8\%$, $350\ \text{K} \le T_{inlet} \le 600\ \text{K}$ and the simulation parameters presented in Table 2.

6. Conclusion

In this paper, the results of a numerical investigation into the thermal and thermodynamic performance of a parabolic trough receiver using a synthetic oil-Al_2O_3 nanofluid are presented. The thermodynamic analysis and optimisation is based on the second law of thermodynamics using the entropy generation minimisation method. The following conclusions can be drawn from the study:

i. The use of nanofluids in the receiver is shown to increase the heat transfer performance by up to 76, 54 and 35% as the volume fraction increases from 0 to 8%, 0 to 6% and 0 to 4% respectively for the range of parameters considered in this study.

ii. It was shown through the thermal efficiency formula that takes into account the increase in heat transfer performance and the corresponding increase in pumping power that the thermal efficiency increases by up to 7.6% at the lowest temperature and flow rate considered. There is also a Reynolds number beyond which further increases in

Reynolds numbers make the thermal efficiency lower than that of a receiver without nanofluids. Flow rates lower than 25 m^3/h were shown to result in significant improvements in thermal efficiency for most volume fractions and temperatures.

iii. From the thermodynamic analysis and optimisation, optimal Reynolds numbers are obtained for which the entropy generation in the receiver is at a minimum. It is certain that there are Reynolds numbers beyond which the use of nanofluids makes no thermodynamic sense. Correlations for these two Reynolds are obtained and presented.

7. Acknowledgements

The support received from the Tshwane University of Technology and the University of Pretoria is duly acknowledged and appreciated. The funding received from the National Research Foundation (NRF), the Translational Engineering Skills Programme (TESP), Stellenbosch University, the South African National Energy Research Institute (SANERI)/South African National Energy Development Institute (SANEDI) at the University of Pretoria, the Council for Scientific and Industrial Research (CSIR), the Energy-efficiency and Demand-side Management (EEDSM) Hub and NAC is also duly acknowledged and appreciated.

REFERENCES

[1] Kalogirou S. Solar energy engineering: processes and systems. 1st ed. Oxford, UK: Elsevier, Academic Press, 2009.

[2] Cecilia B, Aringhoff R, Brakmann G, Geyer M, Teske S. Concentrated solar thermal power-now! Greenpeace/ESTIA/SolarPACES, September 2005:1-47.

[3] Kalogirou SA. Solar thermal collectors and applications. Prog Energ Combust 2004;30:231-95.

[4] Price H, Lüpfert E, Kearney D, Zarza E, Cohen G, Gee R, Mahoney R. Advances in parabolic trough solar power technology. Sol Energy Eng 2002;124:109-25.

[5] SunShot Initiative-High-concentration low cost parabolic trough system for baseload CSP, available at: http://www1.eere.energy.gov/solar/sunshot/csp_baseload_skyfuel.html U S Department of Energy [Last accessed 01.12.2013].

[6] Richter C, Teske S, Short R. Concentrating solar power . Greenpeace/SolarPACES/ESTELA, Global outlook 09, 2009:1-86.

[7] SunShot Initiative available at:http://www1.eere.energy.gov/solar/sunshot/index.html. US Department of Energy [Last accessed 0.1.12.2013].

[8] Schweitzer A, Schiel W, Birkle M, Nava P, Riffelmann K, Wohlfahrt A , Kuhlmann G. ULTIMATE TROUGH® - Fabrication, Erection and Commissioning of the World's Largest Parabolic Trough Collector. Energy Procedia 2014;49:1848-57.

[9] Burkholder F, Kutscher C. Heat loss testing of Schott's 2008 PTR70 parabolic trough receiver. NREL Technical report 2009, NREL/TP - 550-45633:1-58.

[10] Burkholder F, Kutscher C. Heat-loss testing of Solel's UVAC3 parabolic trough receiver. NREL Technical Report 2008, NREL/TP - 550-42394:1-19.

[11] Mwesigye A, Bello-Ochende T, Meyer JP. Numerical investigation of entropy generation in a parabolic trough receiver at different concentration ratios. Energy 2013;53:114-27.

[12] Mwesigye A, Bello-Ochende T, Meyer JP. Minimum entropy generation due to heat transfer and fluid friction in a parabolic trough receiver with non-uniform heat flux at different rim angles and concentration ratios. Energy 2014;73:606-17.

[13] Ravi Kumar K, Reddy KS. Numerical Investigation of Energy-Efficient Receiver for Solar Parabolic Trough Concentrator. Heat Transfer Eng 2008;29:961-72.

[14] Ravi Kumar K, Reddy KS. Thermal analysis of solar parabolic trough with porous disc receiver. Appl Energy 2009;86:1804-12.

[15] Muñoz J, Abánades A. Analysis of internal helically finned tubes for parabolic trough design by CFD tools. Appl Energy 2011;88:4139-49.

[16] Cheng ZD, He YL, Cui FQ. Numerical study of heat transfer enhancement by unilateral longitudinal vortex generators inside parabolic trough solar receivers. Int J Heat Mass Trans 2012;55:5631-41.

[17] Mwesigye A, Bello-Ochende T, Meyer JP. Heat transfer and thermodynamic performance of a parabolic trough receiver with centrally placed perforated plate inserts. Appl Energy 2014;136:989-1003.

[18] Das SK. Nanofluids: science and technology. Hoboken, N.J.: Wiley-Interscience, 2008.

[19] Keblinski P, Eastman JA, Cahill DG. Nanofluids for thermal transport. Materials Today 2005;8:36-44.

[20] Lee S, Choi SUS, Li S, Eastman JA. Measuring thermal conductivity of fluids containing oxide nanoparticles. ASME J Heat Transfer 1999;121:280-289.

[21] Godson L, Raja B, Mohan Lal D, Wongwises S. Enhancement of heat transfer using nanofluids—An overview. Renewable and Sustainable Energy Reviews 2010;14:629-41.

[22] Javadi FS, Saidur R, Kamalisarvestani M. Investigating performance improvement of solar collectors by using nanofluids. Renewable and Sustainable Energy Reviews 2013;28:232-45.

[23] Taylor AR, Phelan EP, Otanicar PT, Walker AC, Nguyen M, Trimble S, Prasher R. Applicability of nanofluids in high flux solar collectors. Renewable Sustainable Energy 2011;023104:1-15.

[24] Waghole DR, Warkhedkar RM, kulkarni VS, Shrivastva RK. Experimental investigations on heat transfer and friction factor of silver nanofliud in absorber/receiver of parabolic trough collector with twisted tape inserts. Energy Procedia 2014;45:558-67.

[25] Sokhansefat T, Kasaeian AB, Kowsary F. Heat transfer enhancement in parabolic trough collector tube using Al2O3/synthetic oil nanofluid. Renewable and Sustainable Energy Reviews 2014;33:636-44.

[26] Bejan A. A study of entropy generation in fundamental convective heat transfer. J Heat Transfer 1979;101:718-25.

[27] Bejan A. Entropy generation minimization: the method of thermodynamic optimization of finite-size systems and finite-time processes. Boca Raton, Fla.: CRC Press, 1996.

[28] ANSYS® Academic research, release 14.5, ANSYS FLUENT, theory guide, ANSYS, Inc.

[29] Shih T, Liou WW, Shabbir A, Yang Z, Zhu J. A new k-ϵ eddy viscosity model for high reynolds number turbulent flows. Comput Fluids 1995;24:227-38.

[30] Herwig H, Kock F. Direct and indirect methods of calculating entropy generation rates in turbulent convective heat transfer problems. Heat and Mass Transfer 2007;43:207-15.

[31] Kock F, Herwig H. Local entropy production in turbulent shear flows: a high-Reynolds number model with wall functions. Int J Heat Mass Trans 2004;47:2205-15.

[32] Kock F, Herwig H. Entropy production calculation for turbulent shear flows and their implementation in cfd codes. Int J Heat Fluid Fl 2005;26:672-80.

[33] Manca O, Mesolella P, Nardini S, Ricci D. Numerical study of a confined slot impinging jet with nanofluids. Nanoscale Res Lett 2011;6:188,276X-6-188.

[34] Li P, Zhang D, Xie Y. Heat transfer and flow analysis of Al2O3–water nanofluids in microchannel with dimple and protrusion. Int J Heat Mass Transfer 2014;73:456-67.

[35] Ho CJ, Chen MW, Li ZW. Numerical simulation of natural convection of nanofluid in a square enclosure: Effects due to uncertainties of viscosity and thermal conductivity. Int J Heat Mass Transfer 2008;51:4506-16.

[36] Roy G, Nguyen CT, Lajoie P. Numerical investigation of laminar flow and heat transfer in a radial flow cooling system with the use of nanofluids. Superlattices and Microstructures 2004;35:497-511.

[37] Maïga SEB, Palm SJ, Nguyen CT, Roy G, Galanis N. Heat transfer enhancement by using nanofluids in forced convection flows. Int J Heat Fluid Flow 2005;26:530-46.

[38] Mahian O, Mahmud S, Heris SZ. Analysis of entropy generation between co-rotating cylinders using nanofluids. Energy 2012;44:438-46.

[39] Buongiorno J, Venerus DC, Prabhat N, McKrell T, Townsend J, Christianson R et al. A benchmark study on the thermal conductivity of nanofluids. J Appl Phys 2009;106.

[40] SYLTHERM 800 heat transfer fluid: product techinical data. http://www.dow.com/heattrans/products/synthetic/syltherm.htm [Last accessed 12.06.2014].

[41] SolTrace optical modelling software, SolTrace 2012;2012.7.9.

[42] Wendelin T. Parabolic trough VSHOT optical characterization in 2005-2006. Parabolic trough technology workshop, February 14-16, 2006, Incline Village, Nevada.

[43] García-Valladares O, Velázquez N. Numerical simulation of parabolic trough solar collector: Improvement using counter flow concentric circular heat exchangers. Int J Heat Mass Trans 2009;52:597-609.

[44] Mullick SC, Nanda SK. An improved technique for computing the heat loss factor of a tubular absorber. Solar Energy 1989;42:1-7.

[45] ANSYS® Academic research, release 14.5, ANSYS FLUENT user's guide, ANSYS, Inc.

[46] Patankar SV, Spalding DB. A calculation procedure for heat, mass and momentum transfer in three-dimensional parabolic flows. Int J Heat Mass Transfer 1972;15:1787-806.

[47] Çengel YA, Ghajar AJ. Heat and mass transfer: fundamentals & applications. 4th ed. New York: McGraw-Hill, 2011.

[48] Blasius PRH. Das Aehnlichkeitsgesetz bei Reibungsvorgangen in Flüssigkeiten. Forschungsheft 1913;131:1-41.

[49] Pak BC, Cho YI. Hydrodynamic and heat transfer study of dispersed fluids with submicron metallic oxide particles. Exp Heat Transfer 1998;11:151-70.

[50] Duangthongsuk W, Wongwises S. An experimental study on the heat transfer performance and pressure drop of TiO2-water nanofluids flowing under a turbulent flow regime. Int J Heat Mass Transfer 2010;53:334-44.

[51] Mwesigye A, Bello-Ochende T, Meyer JP. Multi-objective and thermodynamic optimisation of a parabolic trough receiver with perforated plate inserts. Appl Therm Eng 2015;77:42-56.

[52] Dudley EV, Kolb JG, Mahoney AR, Mancini T, R., Sloan M, Kearney D. Test results: SEGS LS-2 solar collector. Sandia National Laboratory report 1994;SAND94-1884.

[53] Wirz M, Petit J, Haselbacher A, Steinfeld A. Potential improvements in the optical and thermal efficiencies of parabolic trough concentrators. Solar Energy 2014;107:398-414.

List of figures

Figure 15: Entropy generation rate as a function of the Reynolds number and volume fraction at an inlet temperature of: (a) 350 K, (b) 450 K and (c) 550 K

Figure 16: Optimal Reynolds number as a function of volume fraction and inlet temperature

Figure 17: Reynolds number beyond which the use of nanofluid makes no thermodynamic sense, Re_{th} as a function of volume fraction and inlet temperature

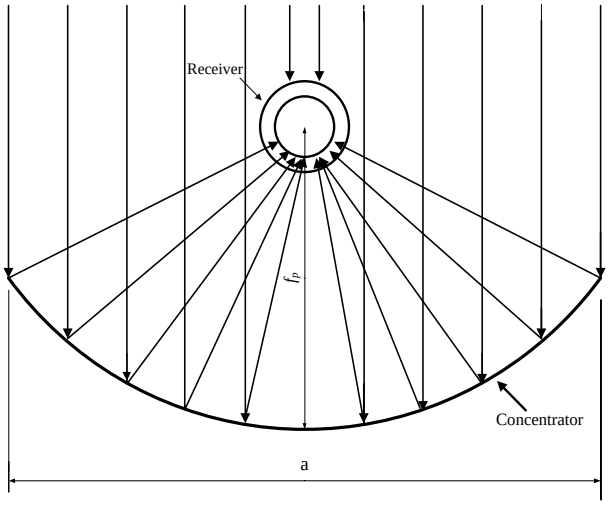

Figure 1

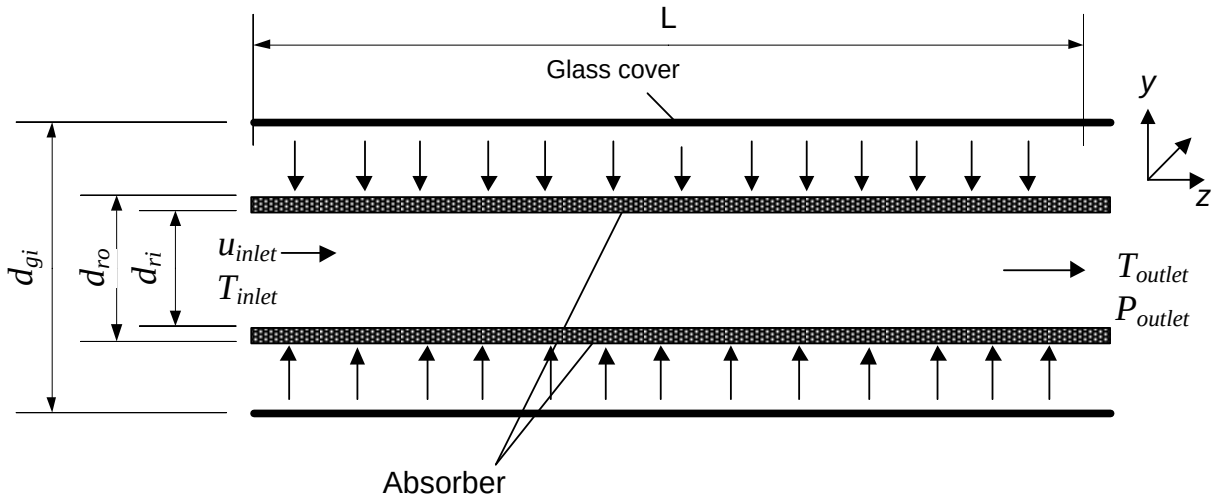

Figure 2(a)

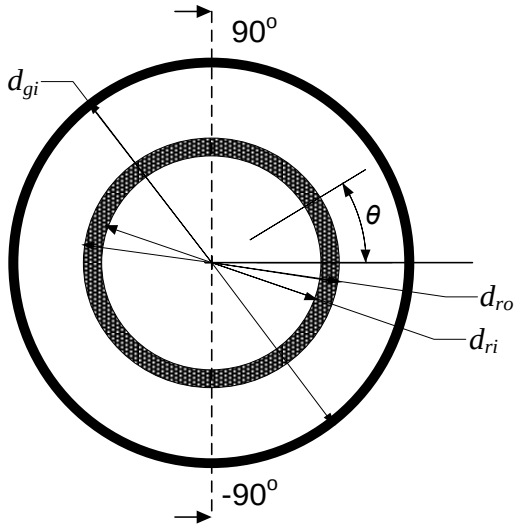

Figure 2(b)

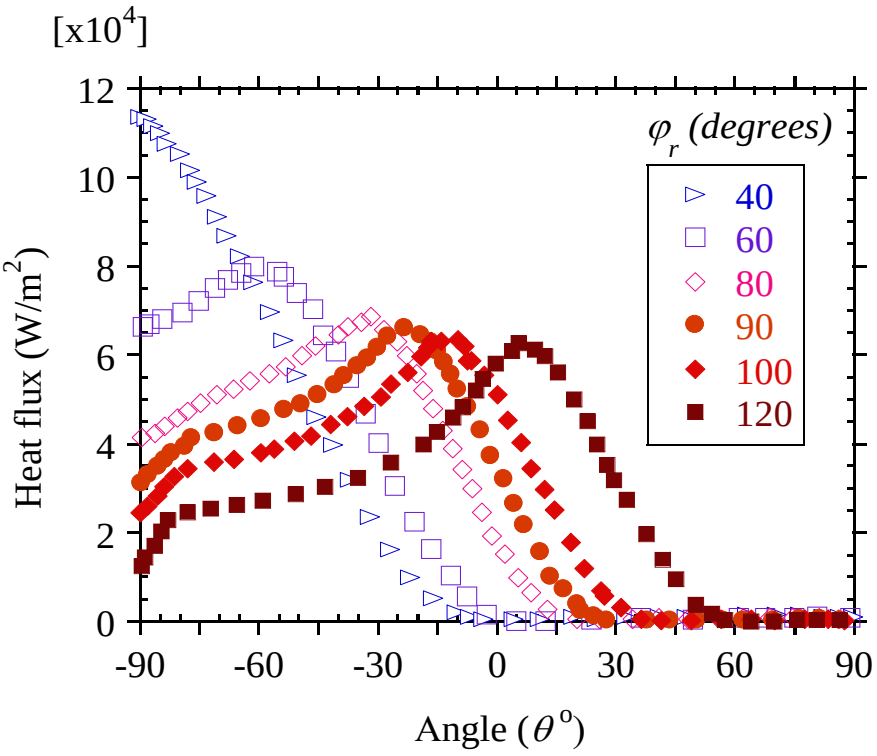

Figure 3(a)

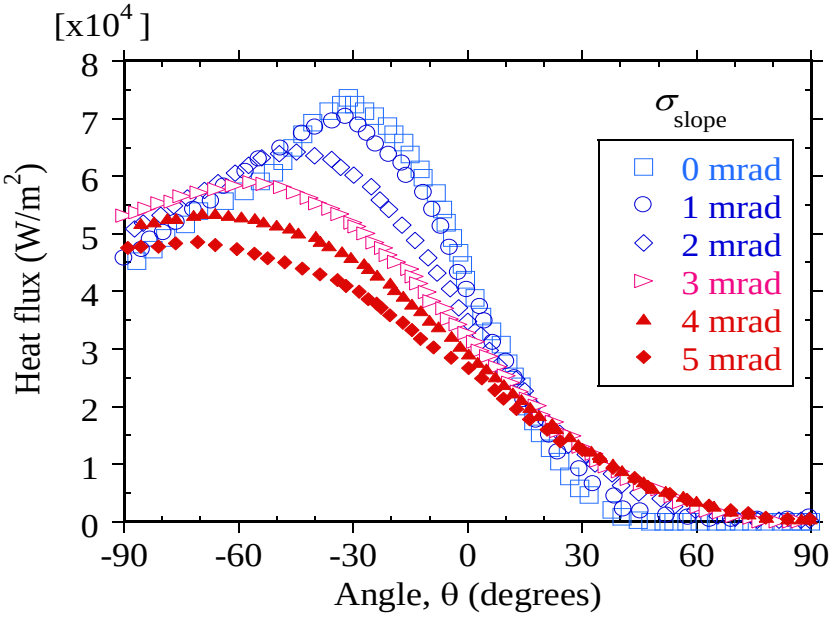

Figure 3(b)

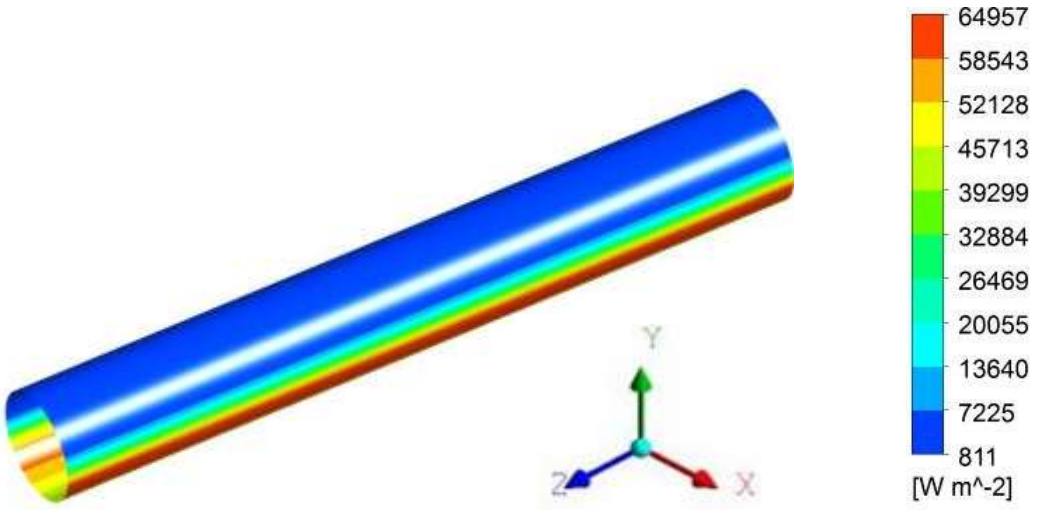
64957
58543
52128
45713
39299
32884
26469
20055
13640
7225
811
[W m^-2]
Y
Z
X

Figure 4

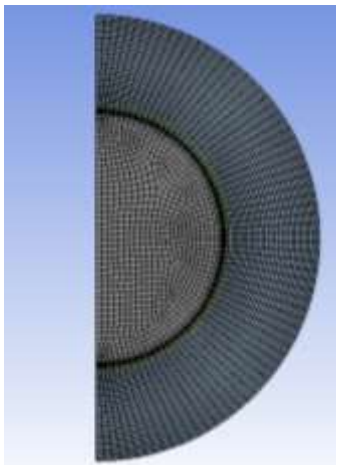

Figure 5(a)

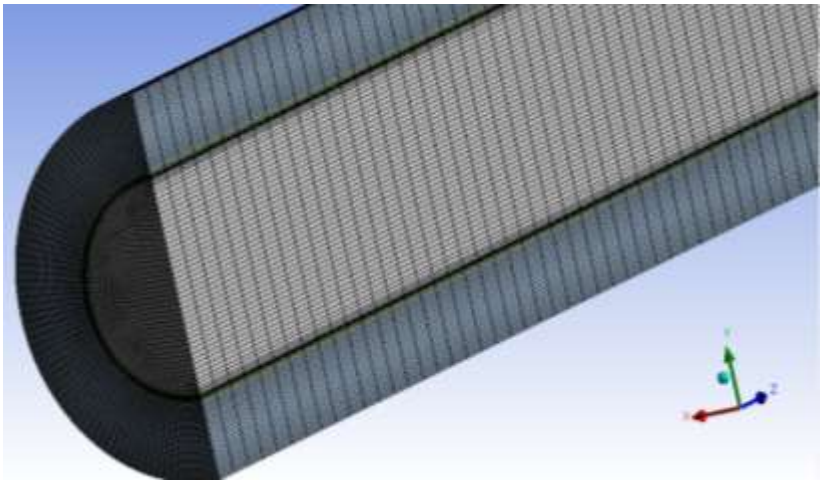

Figure 5(b)

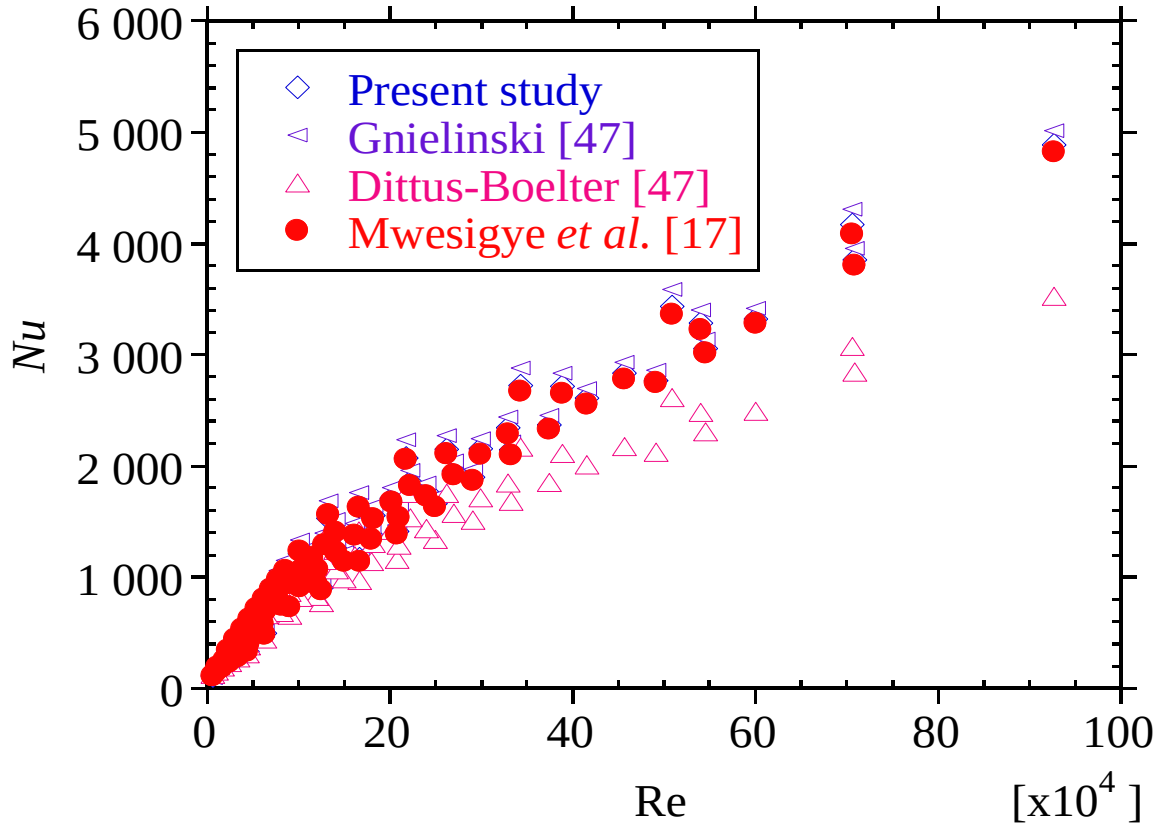

Figure 6

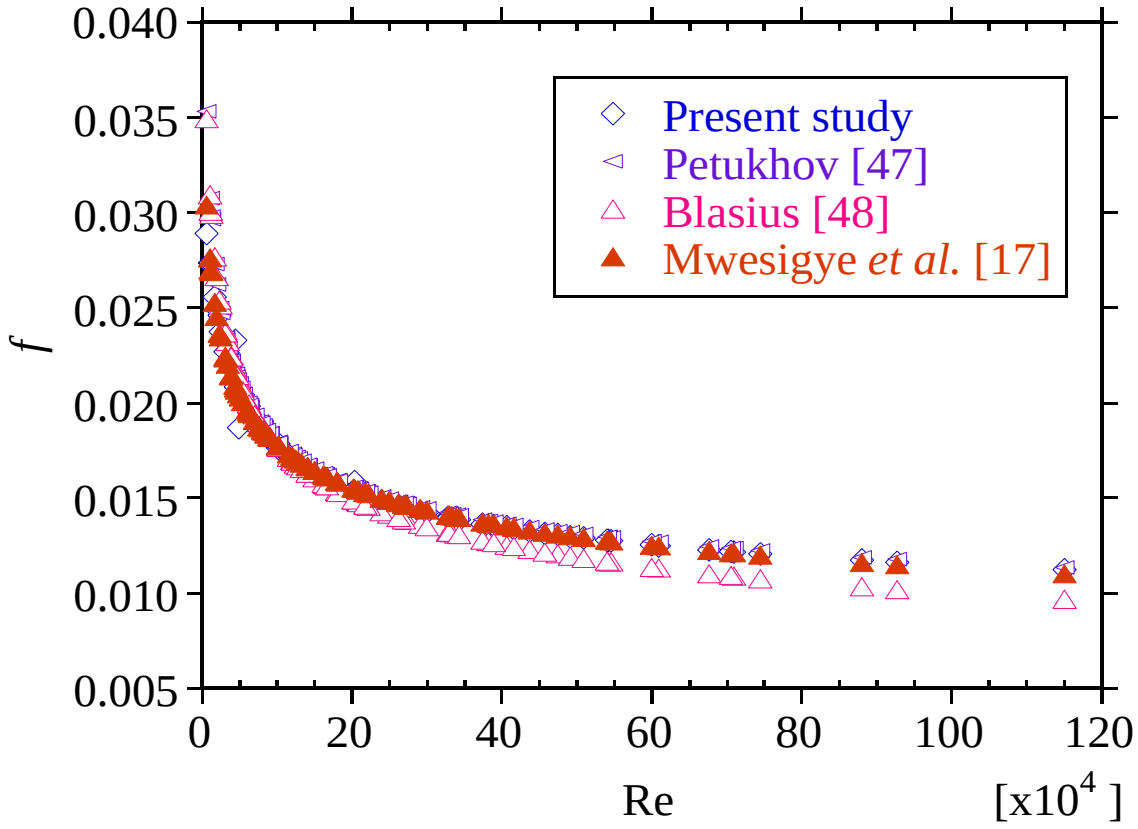
0.040
0.035
0.030
0.025
0.020
0.015
0.010
0.005
f
0
20
40
60
80
100
120
Re
[x10^4]
Present study
Petukhov [47]
Blasius [48]
Mwesigye et al. [17]

Figure 7

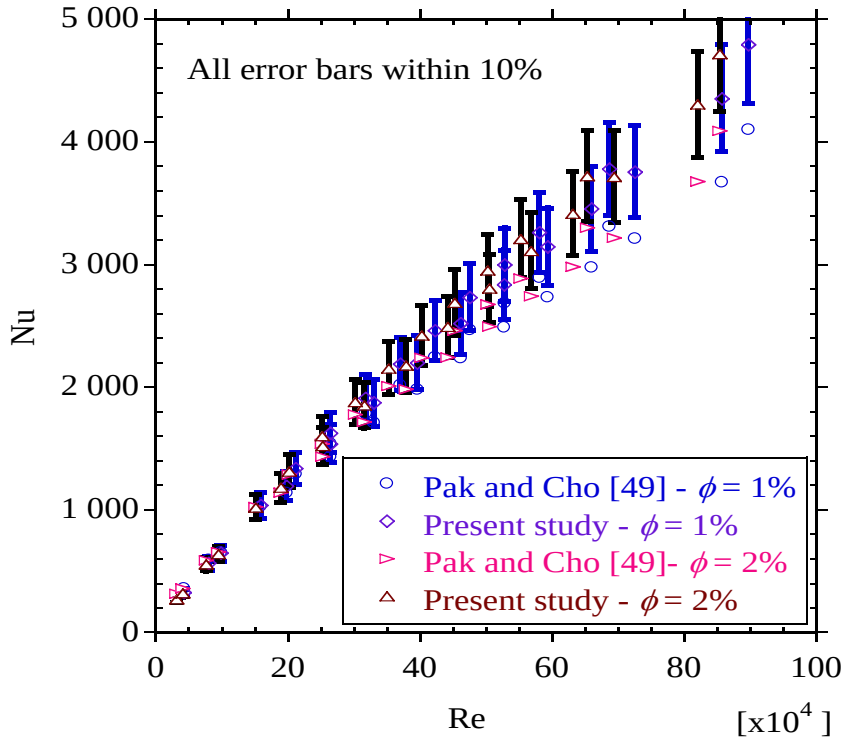

Figure 8 (a)

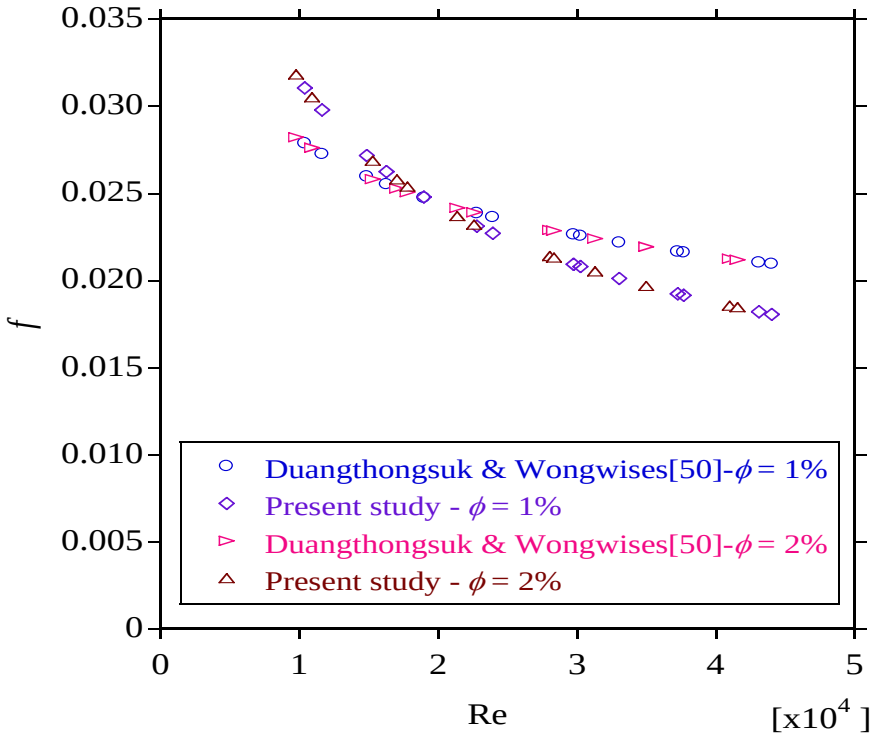

Figure 8 (b)

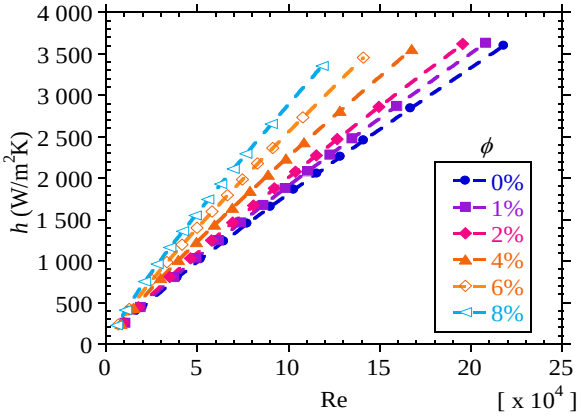

Figure 9(a)

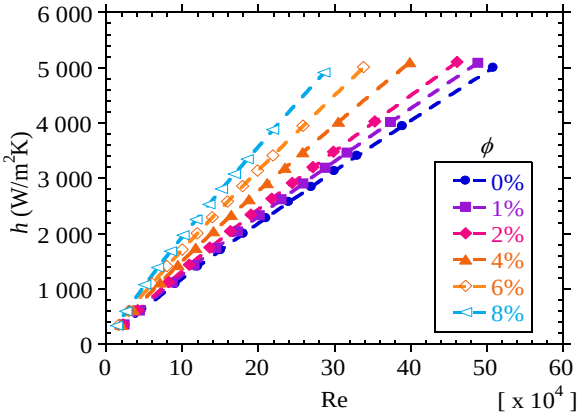

Figure 9(b)

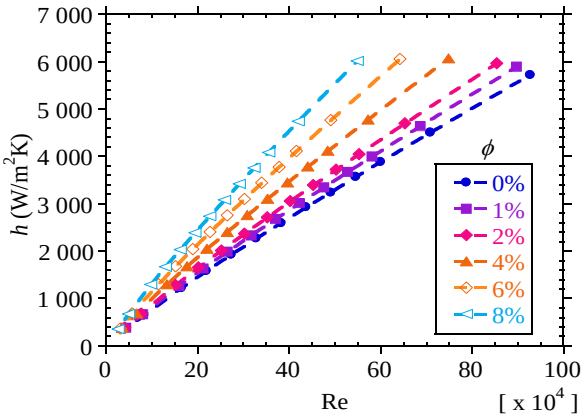

Figure 9(c)

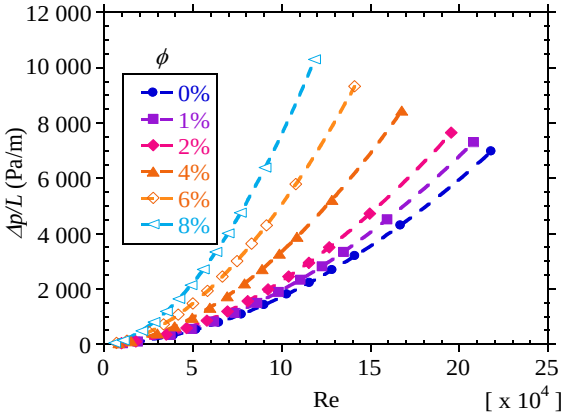

Figure 10(a)

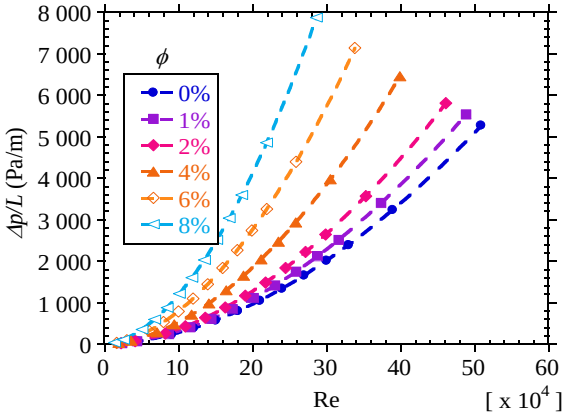

Figure 10(b)

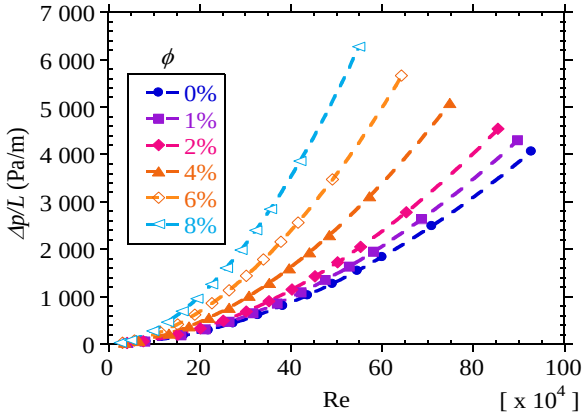

Figure 10(c)

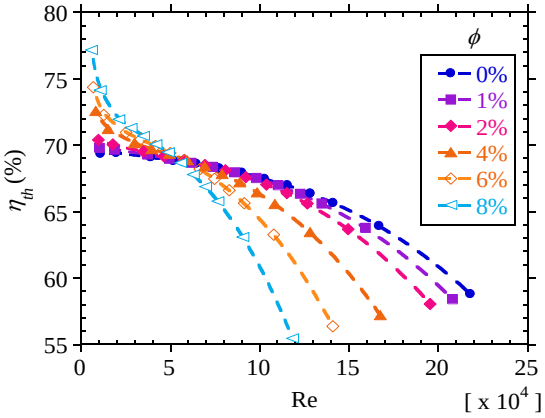

Figure 11(a)

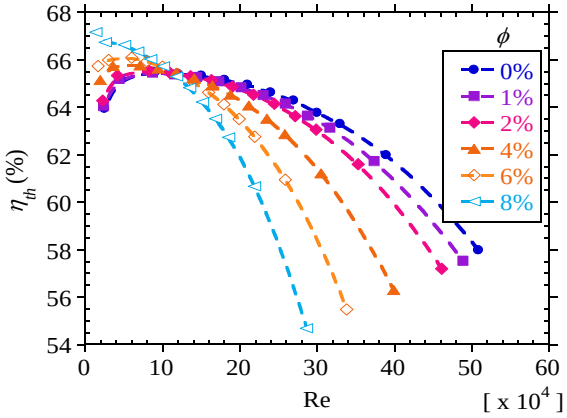

Figure 11(b)

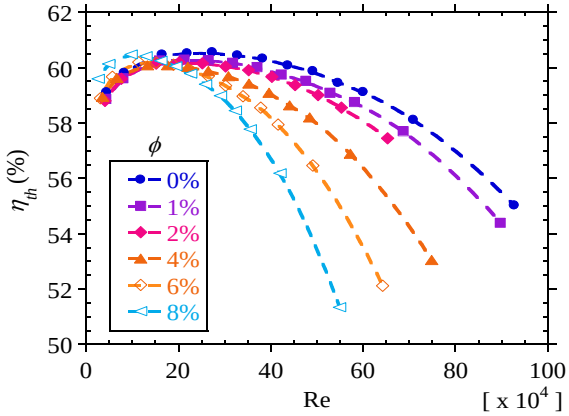

Figure 11(c)

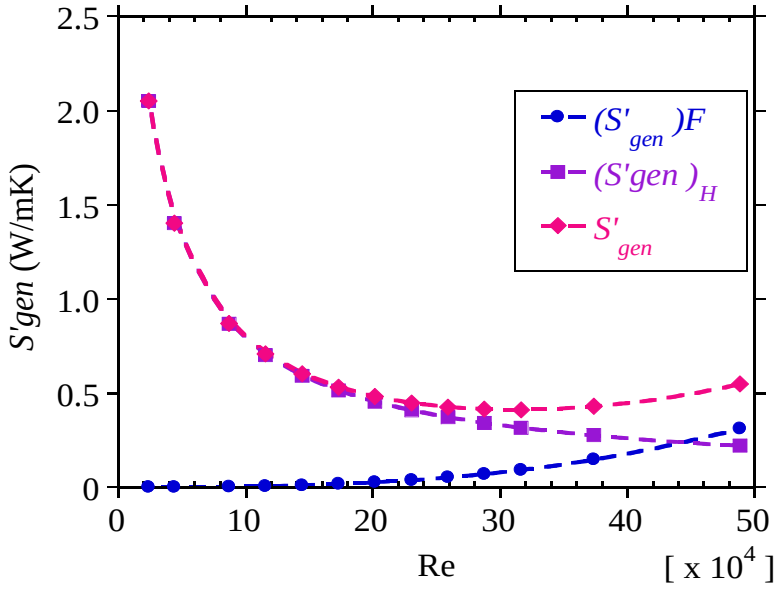

Figure 12

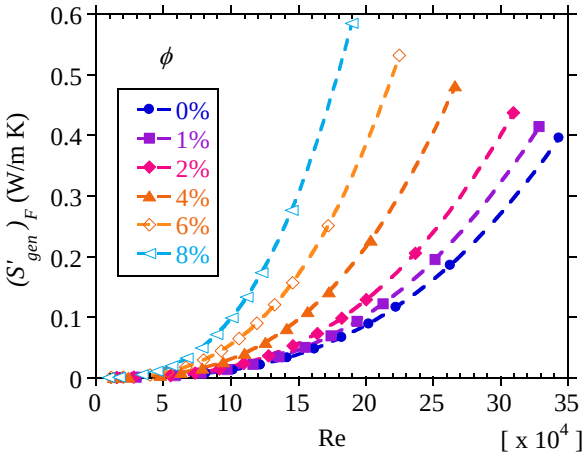

Figure 13(a)

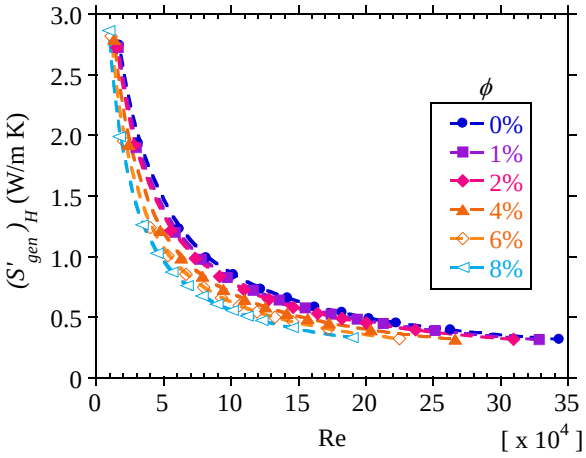

Figure 13(b)

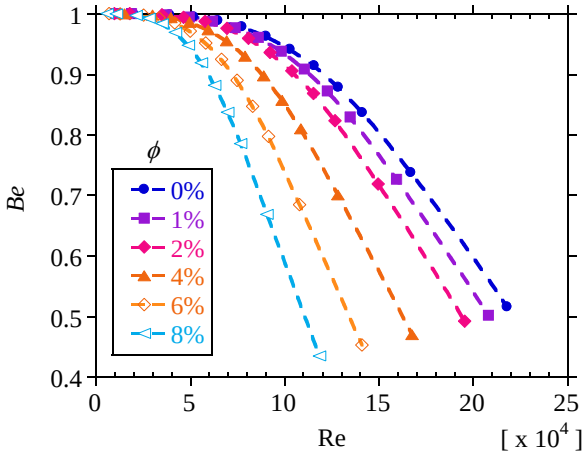

Figure 14(a)

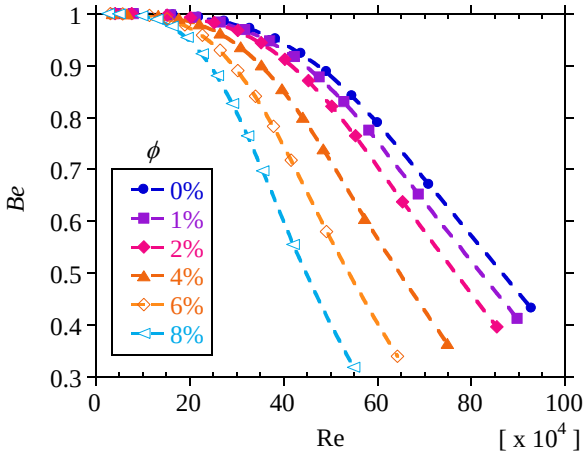

Figure 14(b)

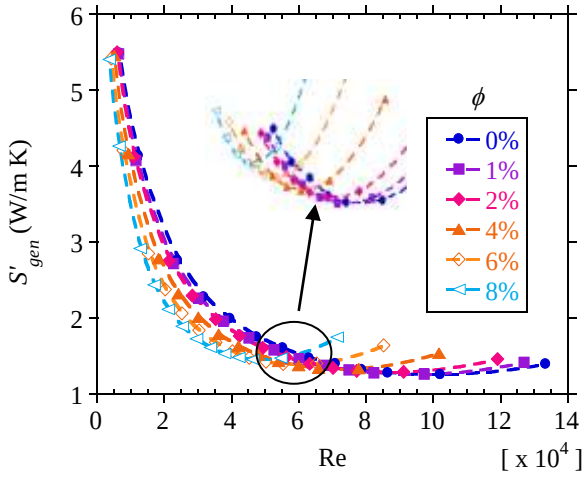

Figure 15(a)

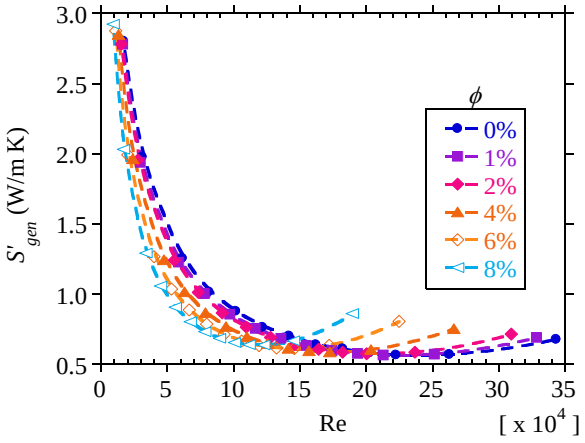

Figure 15(b)

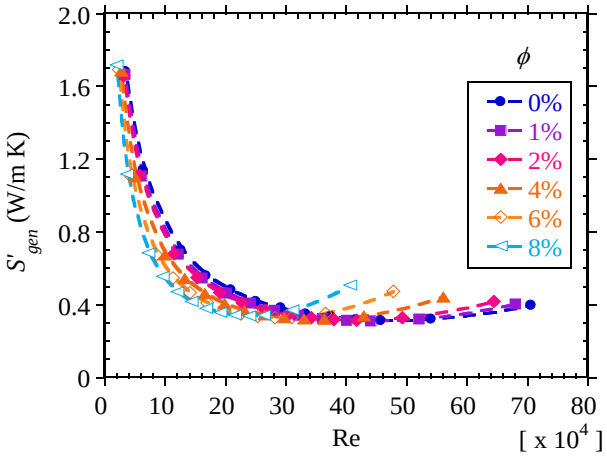

Figure 15(c)

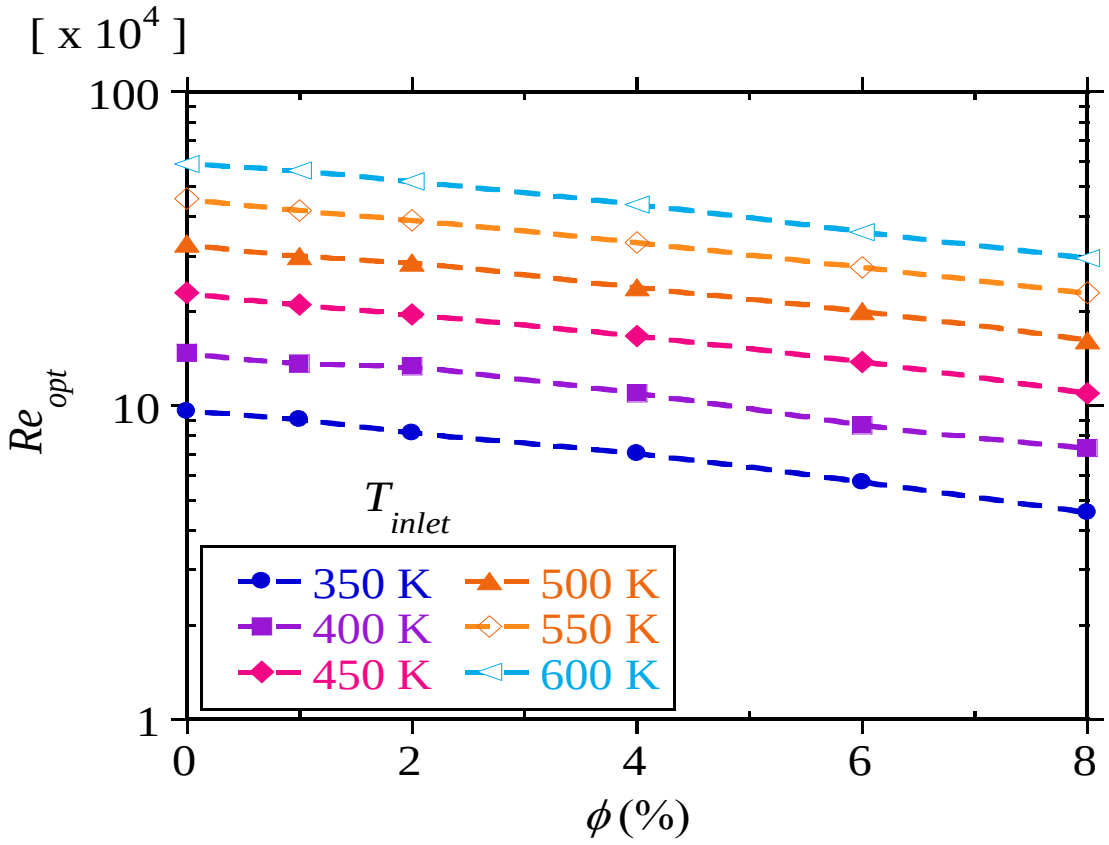
[x 10^4]
100
10
1
Re_opt
0
2
4
6
8
ϕ (%)
T_inlet
350 K
400 K
450 K
500 K
550 K
600 K

Figure 16

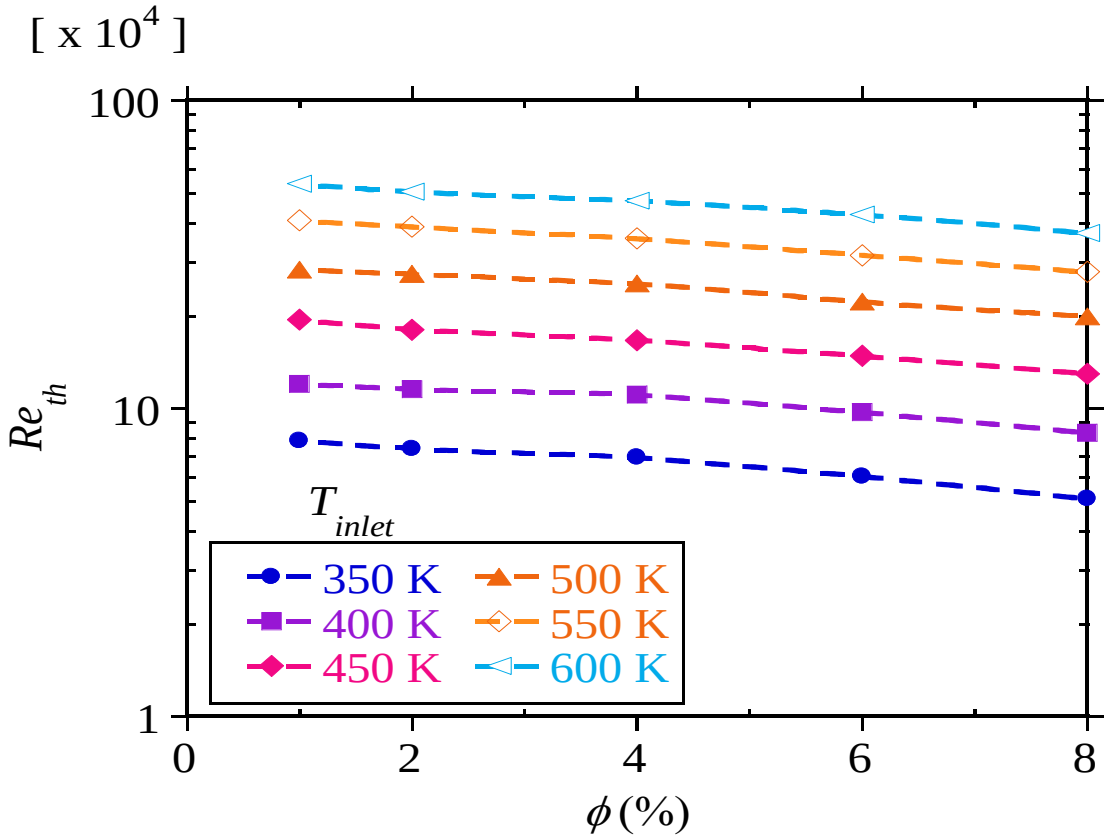
[x 10^4]
100
10
1
Re_th
0
2
4
6
8
ϕ (%)
T_inlet
350 K
400 K
450 K
500 K
550 K
600 K

Figure 17